*J. Fluid Mech.* (2005), *vol.* 539, *pp.* 313–347. © 2005 Cambridge University Press 
doi:10.1017/S0022112005005628 Printed in the United Kingdom

# A study of the Blasius wall jet

By ORI LEVIN[1], VALERY G. CHERNORAY[2], LENNART LÖFDAHL[2] AND DAN S. HENNINGSON[1]

[1]Department of Mechanics, Royal Institute of Technology, SE-100 44 Stockholm, Sweden
[2]Thermo and Fluid Dynamics, Chalmers University of Technology, SE-412 96 Göteborg, Sweden

(Received 12 November 2003 and in revised form 5 January 2005)

A plane wall-jet flow is numerically investigated and compared to experiments. The measured base flow is matched to a boundary-layer solution developing from a coupled Blasius boundary layer and Blasius shear layer. Linear stability analysis is performed, revealing high instability of two-dimensional eigenmodes and non-modal streaks. The nonlinear stage of laminar-flow breakdown is studied with three-dimensional direct numerical simulations and experimentally visualized. In the direct numerical simulation, an investigation of the nonlinear interaction between two-dimensional waves and streaks is made. The role of subharmonic waves and pairing of vortex rollers is also investigated. It is demonstrated that the streaks play an important role in the breakdown process, where their growth is transformed from algebraic to exponential as they become part of the secondary instability of the two-dimensional waves. In the presence of streaks, pairing is suppressed and breakdown to turbulence is enhanced.

## 1. Introduction

### 1.1. *The wall jet*

A wall jet may generally be considered as a flow field that is produced by the injection of a high-velocity fluid in a thin layer close to a surface. The ambient fluid may be either quiescent or moving at a certain velocity, which typically is lower than the velocity of the injected jet. Such flows are of great interest to engineers, for instance in film cooling of gas turbine blades and combustion chambers, in defrosters for automobiles, and in boundary-layer control of airfoils and flaps. Fundamentally, a wall jet may, in principle, be treated as a two-layer flow with an inner region that reaches, in the normal direction, up to the point of maximum velocity and an outer region above. The inner region is most similar to a wall boundary layer and the outer region has a flow pattern that is closely related to a free shear layer. The major characteristics of these layers are different, and in a wall jet, the interaction between these regions forms a complex flow field.

Two-dimensional wall jets have been considered since the mid 1950s and in a classical work by Glauert (1956), it was found that a similarity solution exists for the laminar wall jet. This solution was obtained explicitly and is valid far downstream from the position of the fluid injection. Glauert's solution has provided a good basis for a number of subsequent stability investigations.

### 1.2. *Two-dimensional behaviour*

The temporal linear stability of the Glauert wall jet was examined theoretically by Chun & Schwarz (1967) by solving the Orr–Sommerfeld equation. Bajura &

https://doi.org/10.1017/S0022112005005628 Published online by Cambridge University Press

Szewczyk (1970) performed hot-wire measurements in an air wall jet and confirmed the existence of the Glauert wall jet. Furthermore, the stability of the flow to natural disturbances was studied and the streamwise velocity fluctuation was found to exhibit two large peaks, one peak on each side of the wall jet core. The amplification rate of the outer peak was found to be larger, and hence, the instability of the wall jet is controlled by the outer region. The results are in qualitative agreement with the linear stability theory by Chun & Schwarz (1967). The dominance of the outer region was also reported by Bajura & Catalano (1975), who investigated the whole transition process of a water wall jet. By using flow visualization, they observed the following five stages in natural transition: (i) formation of discrete vortices in the outer region; (ii) vortex pairing in the outer region, resulting in a doubling of the disturbance wavelength, coupled with the possible pairing of vortex-like motions in the inner region; (iii) lift-off of the wall jet into the ambient fluid; (iv) onset of turbulent motion; (v) re-laminarization of the upstream flow, until the next vortex pairing.

By solving the Orr–Sommerfeld equation, Mele *et al.* (1986) clarified the existence of two unstable modes in the wall jet. One mode, unstable at low disturbance frequencies, shows the highest amplitude close to the inflection point in the outer region of the wall jet, while the other mode, unstable at higher frequencies, attains the highest amplitude close to the wall. They concluded that the inviscid instability in the outer region governs the large-scale disturbances while the viscous instability governs the small-scale disturbances close to the wall. Tumin & Aizatulin (1997) numerically investigated the instability and receptivity of a laminar wall jet and concluded that the high-frequency viscous mode can be exited more easily by periodic blowing and suction through the wall than the low-frequency inviscid mode. Cohen, Amitay & Bayly (1992) found a new family of laminar self-similar solutions describing the mean flow of an incompressible two-dimensional wall jet subjected to steady wall blowing or suction. By applying linear stability theory in the temporal framework for the family of solutions, it was shown that blowing stabilizes the inviscid mode while destabilizing the viscous one. The opposite effect was found when suction is applied. These self-similar profiles were later confirmed experimentally by Amitay & Cohen (1993). Amitay & Cohen (1997) investigated the interaction of the two different modes in the wall jet subject to steady wall blowing or suction.

In a low-disturbance environment, the initial stage of the transition process is indeed defined by two-dimensional eigenmodes growing in the outer layer. Two-dimensional direct numerical simulations (DNS) have been successfully employed and the transitional process has been studied (e.g. Gogineni, Visbal & Shih 1999; Seidel & Fasel 2001) for forced laminar wall jets. The simulations demonstrate good agreement with the supporting experiments, at least for the initial stages of transition, where the three-dimensional activity was relatively weak. Seidel & Fasel (2001) adopted a two-dimensional DNS-solver to analyse the effect of periodical forcing by a blowing and suction slot on a laminar wall jet over a heated flat plate. For very low disturbance amplitudes, the simulations show a good agreement with linear stability theory. For an increased amplitude, a strong nonlinear distortion of the mean flow was observed. In particular, the skin friction is reduced markedly, the local maximum velocity is decreased and the wall heat transfer is increased. It was shown that the large structures, generated by the forcing, are the main cause for the strong mean flow distortion of both velocity and temperature. The wall heat transfer was found to increase as large structures entrain cold fluid from the ambient fluid and hot fluid is convected away from the wall.

https://doi.org/10.1017/S0022112005005628 Published online by Cambridge University Press

### 1.3. *Three-dimensional behaviour*

Gogineni *et al.* (1993, 1999) and Gogineni & Shih (1997) investigated a laminar wall jet undergoing transition using particle image velocimetry (PIV). Their results show that the transition process is dominated by formation and development of discrete vortices in both the inner and outer regions and the interaction between them. Three-dimensionality initiated in the outer region spreads to the inner region and the emergence of large three-dimensional structures inside the shear layer triggers the complete breakdown of the flow. The importance of the three-dimensional effects on the transition process has also been numerically demonstrated. Wernz & Fasel (1996, 1997) performed DNS to study the transition process of the wall jet both for two-dimensional and three-dimensional disturbances and found that when forcing of high-amplitude disturbances is introduced, mushroom-shaped structures are ejected from the wall jet into the ambient fluid. Visbal, Gaitonde & Gogineni (1998) investigated the breakdown process in a finite-aspect-ratio wall jet by means of DNS and high-resolution experimental measurements. In the simulation, the experimental base flow was matched to a parabolic profile at the nozzle outlet. In the spanwise direction, an incoming sidewall boundary layer was simulated using a hyperbolic tangent distribution. Two-dimensional forcing was applied by varying the whole base-flow amplitude. They observed a rapid spanwise breakdown of the two-dimensional rollers into streamwise vortices and streaks that start near the sidewalls and propagate toward the midspan of the wall jet.

The primary instability in inflectional base flows such as free shear layers and wall jets is a strong inviscid exponential instability resulting in the roll-up of waves into strong spanwise vortices. These two-dimensional vortices can experience two different types of secondary instability. For low initial three-dimensional excitation, the secondary instability is subharmonic and associated with vortex pairing, like that observed by Bajura & Catalano (1975). If the initial three-dimensional excitation is large enough, a three-dimensional secondary instability is predominant, which changes the path to turbulence.

It is well-known that in a free shear layer, the development of two-dimensional motion is coupled with secondary streamwise coherent structures, see Ho & Huerre (1984), Bernal & Roshko (1986) and Lasheras, Cho & Maxworthy (1986). The three-dimensional instabilities manifest themselves mainly as counter-rotating streamwise vortices and are formed in the braids between the coherent two-dimensional rollers. Numerical studies support these results, see Metcalfe *et al.* (1987) and Balaras, Piomelli & Wallace (2001). The location of the formation of the three-dimensionalities is strongly dependent on the location of the origin and the magnitude of the upstream three-dimensional perturbations. In fact, the observed three-dimensional small scales may destroy the two-dimensional large-scale structures for the case of a high level of random initial disturbances, as is clearly shown by Balaras *et al.* (2001).

### 1.4. *Outline of the paper*

The wall jet constitutes an excellent flow case for studying how a free shear layer and a wall-bounded flow interacts through a detailed investigation of the interplay between two- and three-dimensional structures in the flow breakdown to turbulence. For stability investigations of a high-Reynolds-number wall jet, a description of the laminar base flow is required, and here this flow is analysed using the boundary-layer equations. For the case of a non-interacting boundary layer and top shear layer, a simple solution exists that consists of a coupling of the Blasius boundary layer

https://doi.org/10.1017/S0022112005005628 Published online by Cambridge University Press

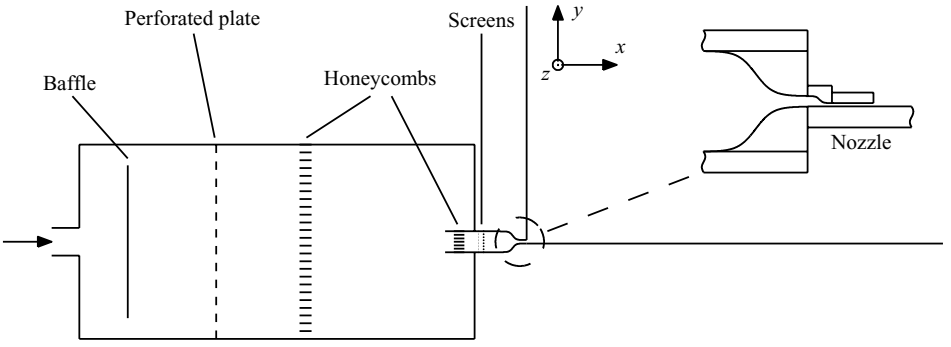



FIGURE 1. Wall-jet facility.

and the Blasius shear layer. Hereinafter, a wall jet of this type and its downstream development is referred to as a *Blasius wall jet*.

In this work, we perform linear stability calculations and highly resolved three-dimensional DNS of the Blasius wall jet and compare the results to experiments. It is discovered that in the experimental wall jet, apart from the two-dimensional waves, almost stationary streaks occur. The streaks interact with the waves and seed the secondary instability. As a result, the breakdown process happens fast, resulting in a short laminar part of the wall jet. Such longitudinal structures are likely to exist in various applications, especially when the wall jet is created through contractions where vorticity is amplified. In § 2, the equipment and methodology of the experiment are described. In § 3, the numerical techniques used are presented and in § 4, the results obtained are presented. Firstly, the measured base flow is matched to the boundary-layer solution. Results from the linear stability calculations for both eigenmodes and non-modal streaks are presented and compared with the experiment. Finally, the nonlinear breakdown process is highlighted by the experiment and examined more closely by analysing the DNS data. The role of subharmonic waves and pairing is also investigated.

## 2. Experimental methods

### 2.1. *Experimental set-up*

All experiments were conducted at Chalmers University of Technology in a wall-jet facility, which is schematically shown in figure 1. The wall jet is formed by the injection of air through a slot and develops over a large horizontal flat plate of 2.1 m in length and 3.2 m in width. This plate is made of wood and coated with a thin plastic laminate. The height of the slot used is 3 mm and the width is 500 mm. A coordinate system is defined in figure 1 with the $x$-axis streamwise, $y$-axis normal to the wall and the $z$-axis in the spanwise direction. Equipped with a vertical back wall of 1.2 m height, located just above the inlet and sidewalls of the same height, the current wall jet can be considered to operate in quiescent surroundings, since the facility is located in a large hall ($15 \times 15 \times 8\,\mathrm{m}^3$) with negligible room draught.

Air is supplied by a centrifugal fan to the settling chamber, which is equipped with flow straightening devices; namely, a baffle, perforated plate, honeycombs and screens. After the settling chamber, the flow enters two smooth contractions of total ratio 36:1. The measured turbulence level of the outlet flow is sufficiently low, less than 0.05 % in the frequency range from 10 Hz to 10 kHz. During the measurements,

https://doi.org/10.1017/S0022112005005628 Published online by Cambridge University Press

the velocity in the middle of the nozzle, $U_0$, is checked by a Pitot–Prandtl tube. The manometer used, FSO510, is also equipped with sensors for temperature and absolute pressure readings.

The streamwise velocity component of the wall-jet flow field is measured by a hot wire, which is monitored by a DANTEC constant-temperature anemometer. A tungsten single-wire boundary-layer probe with a wire diameter and length of 5 μm and 0.7 mm, respectively, is operated at an overheat ratio of 1:8. The hot wire is calibrated in the jet outlet versus the Prandtl tube. Details on the experimental procedure as well as on the measurement equipment used can be found in Chernoray *et al.* (2005). Typically, the calibration resulted in an error of less than 0.5 % for all points in the calibration range. The hot-wire position traversing mechanism is computer controlled and can be completely automated for long experimental runs through the definition of a geometrical mesh of measurement points. Equipped with servo-motors it can sustain an absolute coordinate system with an accuracy of 10 μm in the horizontal directions, and 5 μm in the wall-normal direction. The acquisition system is the IOTech Wavebook 516 sampling module with expansion unit, enabling 16 bit 1 MHz sample and hold with full analogue and digital triggering options. The software used to control the sampling and saving of data files is linked into a program for automated, triggered flow measurements using the traverse system and a pre-defined mesh of sampling points. The distance between the hot wire and the wall is measured using an 'electro-optical' method and is checked before every experimental run. To employ this method, a strip of electrically conductive foil is glued onto the surface and when one probe prong touches the surface an electric circuit is closed. The distance between the wire and the wall when the prong touches the surface is measured optically in this position. It should be pointed out that the wall-distance measurements are performed before the hot-wire calibration.

### 2.2. *Artificial disturbances*

To use the advantages of a controlled experiment and to study the development of two-dimensional waves and stationary longitudinal streaks in detail, disturbances are introduced in the flow artificially.

Time-periodic two-dimensional waves are excited by a loudspeaker situated about two metres downstream of the nozzle outlet. The signal for the loudspeaker of controlled frequency and amplitude is generated by an analogue output board in a computer and an external amplifier unit. The frequency of the artificial disturbances is chosen to be 1221 Hz, which is close to the natural flow frequency and detuned off 50 Hz of the power network. The measurement of the linear instability waves is performed in a region starting at about one hydrodynamic wavelength downstream of the nozzle outlet and prior to the downstream distance where significant nonlinear interactions occur. Such recommendations can be found in the review by Ho & Huerre (1984) for shear layers and are based mostly on the fact that instability waves are influenced by the solid edge in a near-field region. It is also recommended that the acoustic wavelength should be large enough for the assurance of the wave two-dimensionality, and this length is about 0.3 m for the mentioned frequency of 1221 Hz. Before the experiment, the two-dimensionality of the base flow and that of the excited waves is carefully checked through measurements and visualizations. To obtain the amplitude and phase information of the signal, fast Fourier transform (FFT) is applied to the velocity time traces, see Chernoray *et al.* (2005) for details.

Stationary longitudinal streaks are introduced in the flow by fine roughness elements of controlled geometry and a typical height of 40 μm. The roughness elements are

https://doi.org/10.1017/S0022112005005628 Published online by Cambridge University Press

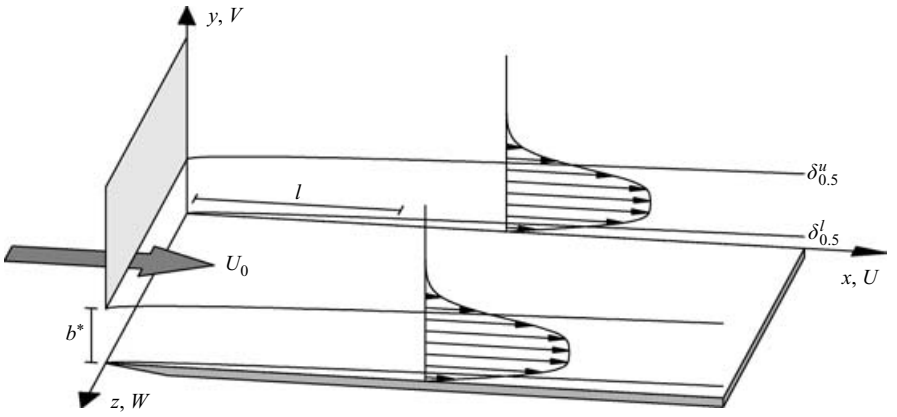



FIGURE 2. Plane wall-jet flow.

positioned at the orifice of the wall jet onto the inner surface of the top lip of the nozzle. To introduce a streaky pattern of a single spanwise scale, typically an array of five uniformly distributed roughness elements is used. It is decided to introduce five different streak scales, and accordingly five groups of humps are positioned on the nozzle. As a result, nearly sinusoidal mean flow modulation is obtained after a short distance downstream of the nozzle outlet. The evaluation of the streaks is performed by measurements of $(y, z)$-velocity planes of two or three spanwise wavelengths. A cross-sectional plane for each scale is taken with constant steps in the $y$-direction of 0.15 mm and 0.5 mm in the $z$-direction, and the corresponding number of points for each plane is 20 in the wall-normal extent and from 12 to 30 in the spanwise extent, depending on the spanwise streak scale. Subsequently, the undisturbed base flow is subtracted and the remaining stationary disturbance is decomposed into spanwise modes using FFT.

During the measurements, the output signal from the anemometer is amplified and digitized; post-processing is done using the software package Matlab.

## 3. Numerical solution methods

### 3.1. *Scaling*

Consider an incompressible wall jet over a flat plate as illustrated in figure 2. Through a slot with height $b^*$, fluid with exit velocity $U_0$ is blown tangentially along a wall. The scalings are originating from the boundary-layer approximations. The streamwise coordinate $x$ is scaled with the length scale $l$, which is a fixed distance from the slot. The wall-normal and spanwise coordinates $y$ and $z$, respectively, are scaled with the boundary-layer parameter $\delta = \sqrt{\nu l/U_0}$, where $\nu$ is the kinematic viscosity of the fluid. The streamwise velocity $U$ is scaled with $U_0$, while the wall-normal and spanwise velocities $V$ and $W$, respectively, are scaled with $U_0\delta/l$. The pressure $P$ is scaled with $\rho U_0^2\delta^2/l^2$, where $\rho$ is the density of the fluid, and the time $t$ is scaled with $l/U_0$. The Reynolds numbers used here are defined as $Re_l = U_0 l/\nu$ and $Re_\delta = U_0\delta/\nu$. It is useful to note the relations $l/\delta = Re_\delta = \sqrt{Re_l}$.

### 3.2. *Linear disturbance equations*

The well-known technique based on the parabolized stability equations (PSE) (Bertolotti, Herbert & Spalart 1992; Herbert 1997) deals with the spatial evolution of

https://doi.org/10.1017/S0022112005005628 Published online by Cambridge University Press

exponentially growing eigenmodes. These equations are scaled with a suitable scaling for modal waves, e.g. the streamwise and normal disturbance velocities are assumed to be of the same order. However, in the last decade there has been an increasing interest in the algebraically growing non-modal Klebanoff modes (Klebanoff 1971; Westin *et al.* 1994; Andersson, Berggren & Henningson 1999; Luchini 2000). The two growth scenarios are associated with different scales. The governing equations for non-modal disturbances are scaled with the boundary-layer scalings (see Andersson *et al.* 1999). Here we summarize a set of stability equations valid for both algebraically and exponentially growing disturbances, given by Levin & Henningson (2003). For further details, see that investigation.

We want to study the linear stability of a high-Reynolds-number flow. The non-dimensional Navier–Stokes equations for an incompressible flow are linearized around a two-dimensional, steady base flow $(U(x, y),\ V(x, y),\ 0)$ to obtain the stability equations for the spatial evolution of three-dimensional time-dependent disturbances $(u(x, y, z, t),\ v(x, y, z, t),\ w(x, y, z, t),\ p(x, y, z, t))$. The disturbances, that are scaled as the base flow, are taken to be periodic in the spanwise direction and time. This allows us to assume solutions of the form

$$f = \hat{f}(x, y) \exp\left(\mathrm{i}Re_\delta \int_{x_0}^{x} \alpha(x)\,\mathrm{d}x + \mathrm{i}\beta z - \mathrm{i}\omega t\right), \tag{3.1}$$

where $f$ represents either one of the disturbances $u$, $v$, $w$ or $p$. The complex streamwise wavenumber $\alpha$ captures the fast wavelike variation of the modes and is therefore scaled with $1/\delta$, but $\alpha$ itself is assumed to vary slowly with $x$. The $x$-dependence in the amplitude function $\hat{f}$ includes the weak variation of the disturbances. The real spanwise wavenumber $\beta$ and the real disturbance angular frequency $\omega$ are scaled in a consistent way with $z$ and $t$, respectively. Introducing (3.1) in the linearized Navier–Stokes equations and neglecting third-order terms in $1/Re_\delta$ or higher, we arrive at the parabolized stability equations in boundary-layer scalings

$$\hat{u}_x + \mathrm{i}Re_\delta \alpha \hat{u} + \hat{v}_y + \mathrm{i}\beta\hat{w} = 0, \tag{3.2a}$$

$$(U_x + \mathrm{i}Re_\delta \alpha U - \mathrm{i}\omega)\hat{u} + U\hat{u}_x + V\hat{u}_y + U_y\hat{v} + \frac{\hat{p}_x}{Re_\delta^2} + \frac{\mathrm{i}\alpha\hat{p}}{Re_\delta} = \hat{u}_{yy} - k^2\hat{u}, \tag{3.2b}$$

$$(V_y + \mathrm{i}Re_\delta \alpha U - \mathrm{i}\omega)\hat{v} + U\hat{v}_x + V_x\hat{u} + V\hat{v}_y + \hat{p}_y = \hat{v}_{yy} - k^2\hat{v}, \tag{3.2c}$$

$$(\mathrm{i}Re_\delta \alpha U - \mathrm{i}\omega)\hat{w} + U\hat{w}_x + V\hat{w}_y + \mathrm{i}\beta\hat{p} = \hat{w}_{yy} - k^2\hat{w}, \tag{3.2d}$$

where $k^2 = \alpha^2 + \beta^2$. All the terms are generally of the first or the second order except the $\hat{p}_x/Re_\delta^2$-term, in (3.2*b*), which is of the third order for the algebraic instability problem and the $V_x\hat{u}$-term, in (3.2*c*), which is of the third order for the exponential instability problem. Both of these terms, however, have to be included in a general formulation of the problem. Unfortunately, the $\hat{p}_x/Re_\delta^2$-term introduces numerical instability, setting a lower limit of the streamwise step size (Li & Malik 1994), as is the case for all PSE-formulations.

We are interested in solutions subject to no-slip conditions at the plate and vanishing at the wall-normal position $y_{max}$ well outside the wall jet. The boundary conditions in the wall-normal direction can then be written

$$\left.\begin{aligned} \hat{u} = \hat{v} = \hat{w} = 0 \quad \text{at} \quad y = 0, \\ \hat{u} = \hat{v} = \hat{w} = 0 \quad \text{at} \quad y = y_{max}. \end{aligned}\right\} \tag{3.3}$$

https://doi.org/10.1017/S0022112005005628 Published online by Cambridge University Press

The set of equations is nearly parabolic in the streamwise coordinate and is marched forward from an initial position $x_0$ to a final position $x_1$. Given the initial conditions

$$\hat{u} = \hat{u}_0(y), \quad \hat{v} = \hat{v}_0(y), \quad \hat{w} = \hat{w}_0(y) \quad \text{at} \quad x = x_0, \tag{3.4}$$

the wavenumber $\beta$ and the angular frequency $\omega$, the initial-boundary-value problem is solved from $x_0$ to $x_1$ to obtain the downstream development of the disturbance.

The disturbance growth is generally measured by the average change in the kinetic energy of the fluid. In spatially evolving investigations, a commonly used quantity to represent this change is the disturbance energy defined as

$$E(x, \beta, \omega, Re_l) = \int_0^{y_{max}} (Re_l|u|^2 + |v|^2 + |w|^2)\,\mathrm{d}y = \hat{E}\mathrm{e}^{\theta}, \tag{3.5}$$

where

$$\hat{E} = \int_0^{y_{max}} (Re_l|\hat{u}|^2 + |\hat{v}|^2 + |\hat{w}|^2)\,\mathrm{d}y, \quad \theta = -2Re_\delta \int_{x_0}^{x} \alpha_\mathrm{i}\,\mathrm{d}x. \tag{3.6}$$

3.2.1. *Exponential growth*

Here we consider solutions to (3.2)–(3.4) associated with wavelike disturbances, i.e. where $\alpha$ in the phase function in (3.6) is order unity. As both the amplitude and phase functions depend on $x$, one more equation is required. We require that both the amplitude function and the wavenumber $\alpha$ change slowly in the streamwise direction, and specify a normalization condition on the amplitude function

$$\int_0^{y_{max}} (Re_l\overline{\hat{u}}\hat{u}_x + \overline{\hat{v}}\hat{v}_x + \overline{\hat{w}}\hat{w}_x)\,\mathrm{d}y = 0, \tag{3.7}$$

where the bar denotes complex conjugate. Other conditions are possible and are presented in the paper by Bertolotti *et al.* (1992). The normalization condition specifies how much growth and sinusoidal variation are represented by the amplitude and phase function, respectively. The stability problem (3.2)–(3.4) and (3.7) have to be solved iteratively in each streamwise step. The numerical method solving the stability equations is based on a spectral collocation method involving Chebyshev polynomials. Details about the numerical scheme can be found in Andersson *et al.* (1999) and Hanifi, Schmid & Henningson (1996). The initial condition (3.4) is taken as the least stable eigenfunction of the Orr–Sommerfeld and Squire equations with corresponding eigenvalue $\alpha(x_0)$. Since the initial condition does not capture non-parallel effects, there will be a region in the beginning of the domain that includes some errors (e.g. see figure 9). The size of these errors and the length of this region are dependent of the type of base flow and how non-parallel it is.

3.2.2. *Optimal disturbances*

Now we consider solutions to (3.2)–(3.4) with $\alpha = 0$, giving rise to disturbances with weak streamwise variations. We are interested in maximizing the disturbance energy (3.5), at the downstream position $x_1$, by optimizing the initial disturbance at $x_0$ with given initial energy. That is, we want to maximize the disturbance growth defined by

$$G(x_0, x_1, \beta, \omega, Re_l) = \frac{E(x_1)}{E(x_0)}. \tag{3.8}$$

When going to the limit of large Reynolds number, the maximum growth will, because of the difference in order between the terms in the disturbance energy (3.5), be obtained for initial disturbances with a zero streamwise velocity component. Furthermore,

https://doi.org/10.1017/S0022112005005628 Published online by Cambridge University Press

provided that $\hat{u}_1$ is non-zero, $\hat{v}_1$ and $\hat{w}_1$ can be neglected and the Reynolds-number-independent growth can be simplified to

$$\overline{G} = \lim_{Re_l \to \infty} \frac{G}{Re_l} = \frac{\displaystyle\int_0^{y_{max}} |\hat{u}_1|^2 \, \mathrm{d}y}{\displaystyle\int_0^{y_{max}} (|\hat{v}_0|^2 + |\hat{w}_0|^2) \, \mathrm{d}y} = \frac{(\hat{u}_1, \hat{u}_1)_u}{(\boldsymbol{q}, \boldsymbol{q})_q}. \tag{3.9}$$

The last identity defines the appropriate inner products, where $\boldsymbol{q} = (\hat{v}_0, \hat{w}_0)^T$. The optimization problem in the large-Reynolds-number limit is defined by maximizing (3.9) and concerns the optimization of the initial disturbance $\boldsymbol{q}$ for given values of $x_0$, $x_1$, $\beta$ and $\omega$. Details about the derivation of the optimization procedure can be found in the Appendix and in Levin & Henningson (2003) and details about the numerical scheme is given in Andersson *et al.* (1999) and Hanifi *et al.* (1996). The numerical method solving the forward problem (3.2)–(3.4) and the backward problem (A 5)–(A 7) is based on a spectral collocation method involving Chebyshev polynomials.

### 3.3. *DNS techniques*

#### 3.3.1. *Numerical methods*

The numerical code (see Lundbladh *et al.* 1999) uses spectral methods to solve the three-dimensional time-dependent incompressible Navier–Stokes equations. The discretization in the streamwise and spanwise directions make use of Fourier series expansions, which enforces periodic solutions. The discretization in the normal direction is represented with Chebyshev polynomial series. A pseudospectral treatment of the nonlinear terms is used. The time advancement used is a second-order Crank–Nicolson method for the linear terms and a four-step low-storage third-order Runge–Kutta method for the nonlinear terms. Aliasing errors arising from the evaluation of the pseudospectrally convective terms are removed by dealiasing by padding and truncation using the 3/2-rule when the FFTs are calculated in the wall-parallel planes. In the normal direction, it has been found that increasing the resolution is more efficient than the use of dealiasing.

Flows such as boundary layers and wall jets are spatially growing and to fulfil the necessary periodic boundary condition in the streamwise direction, required by the spectral discretization, a fringe region (see Nordström, Nordin & Henningson 1999) is added in the downstream end of the computational domain. In this region, the function $\lambda(x)$ is smoothly raised from zero and the flow is forced to a desired solution $\boldsymbol{v}$ in the following manner

$$\frac{\partial \boldsymbol{u}}{\partial t} = NS(\boldsymbol{u}) + \lambda(x)(\boldsymbol{v} - \boldsymbol{u}) + \boldsymbol{g}, \tag{3.10}$$

$$\nabla \cdot \boldsymbol{u} = 0, \tag{3.11}$$

where $\boldsymbol{u}$ is the solution vector and $NS(\boldsymbol{u})$ the right-hand side of the (unforced) momentum equations. Both $\boldsymbol{g}$, which is a disturbance forcing, and $\boldsymbol{v}$ may depend on the three spatial coordinates and time. The forcing vector $\boldsymbol{v}$ is smoothly changed (blended) from the undisturbed wall-jet solution of the boundary-layer equations at the beginning of the fringe region to the prescribed inflow velocity vector, which is the Blasius wall jet shown in figure 3(*a*). In the case of forcing a disturbance in the flow, it is also added to the forcing vector in the end of the fringe region. The fringe

https://doi.org/10.1017/S0022112005005628 Published online by Cambridge University Press

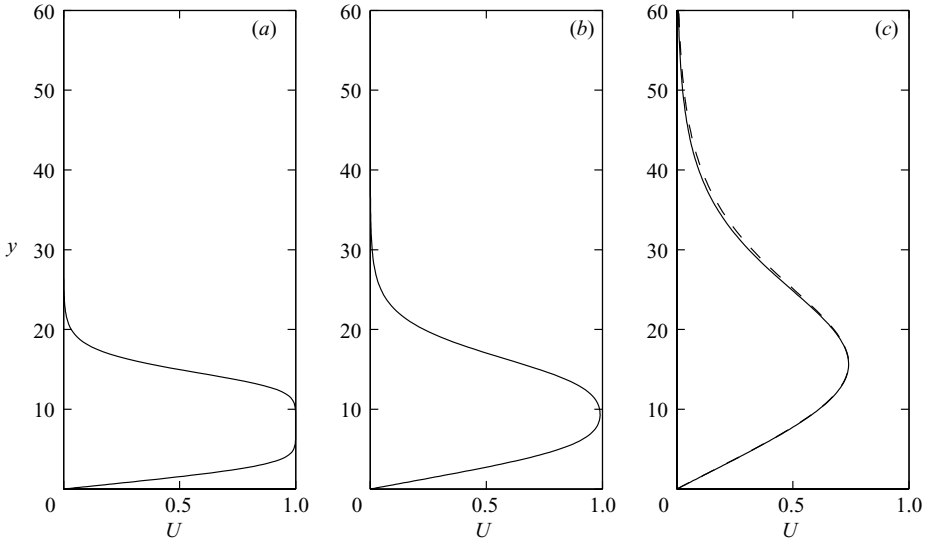



FIGURE 3. Streamwise development of the Blasius wall jet calculated with the boundary-layer equations. (*a*) $x=1$, (*b*) 3.14, (*c*) 20. Far downstream, the solution approaches a Glauert similarity solution evolving from a different virtual origin. The Glauert solution (– – –) is shown for comparison in (*c*).

function is conveniently written as

$$\lambda(x) = \lambda_{max}\left[S\left(\frac{x - x_{start}}{\Delta_{rise}}\right) - S\left(\frac{x - x_{end}}{\Delta_{fall}} + 1\right)\right], \tag{3.12}$$

where $\lambda_{max}$ is the maximum strength of the damping, $x_{start}$ and $x_{end}$ are the start and end of the fringe region, respectively, and $\Delta_{rise}$ and $\Delta_{fall}$ are the rise and fall distance of the damping function. $S(\xi)$ is a smooth step function with continuous derivatives of all orders defined by

$$S(\xi) = \begin{cases} 0, & \xi \leqslant 0, \\ 1\Big/\left[1 + \exp\left(\dfrac{1}{\xi - 1} + \dfrac{1}{\xi}\right)\right], & 0 < \xi < 1, \\ 1, & \xi \geqslant 1. \end{cases} \tag{3.13}$$

This method damps disturbances flowing out of the physical region and smoothly transforms the flow to the desired inflow state, with a minimal upstream influence (Nordström *et al.* 1999).

At the wall, a no-slip boundary condition is set and at the free-stream position $y_{max}$, a generalized boundary condition is applied in Fourier space with different coefficients for each wavenumber. It is non-local in physical space and takes the form

$$\frac{\partial \hat{\boldsymbol{u}}}{\partial y} + k\hat{\boldsymbol{u}} = \frac{\partial \hat{\boldsymbol{v}}_0}{\partial y} + k\hat{\boldsymbol{v}}_0, \tag{3.14}$$

where $\hat{\boldsymbol{u}}$ is the Fourier transform of $\boldsymbol{u}$. Here, $\boldsymbol{v}_0$ denotes the blended wall-jet solution of the boundary-layer equations taken as the initial condition and $\hat{\boldsymbol{v}}_0$ its Fourier transform. In the spanwise direction, periodic boundary condition is set.

https://doi.org/10.1017/S0022112005005628 Published online by Cambridge University Press

3.3.2. *Disturbance generation and numerical parameters*

The present numerical implementation provides several possibilities for disturbance generation. Disturbances can be included in the desired solution $\boldsymbol{v}$, thereby forcing them in the fringe region, by a body force $\boldsymbol{g}$ and by blowing and suction at the wall through non-homogeneous boundary conditions.

To study the instability and interaction of time-periodic two-dimensional waves $\boldsymbol{v}_w$ and stationary longitudinal streaks $\boldsymbol{v}_s$, the velocity fields are added to the blended Blasius wall-jet solution $\boldsymbol{v}_0$ to give a forcing vector of the form $\boldsymbol{v} = \boldsymbol{v}_0 + \boldsymbol{v}_w + \boldsymbol{v}_s$. The waves and streaks can then be forced in the fringe region. The two-dimensional waves $\boldsymbol{v}_w = (u, v, 0)$ are taken from solutions of the parabolized stability equations (3.2) with $\beta = 0$. The vector, which can be derived from (3.1) takes the form

$$\boldsymbol{v}_w = \boldsymbol{f}_c \cos\omega t + \boldsymbol{f}_s \sin\omega t, \tag{3.15}$$

where

$$\boldsymbol{f}_c = (\hat{\boldsymbol{f}}_{\mathrm{r}} \cos a_{\mathrm{r}} - \hat{\boldsymbol{f}}_{\mathrm{i}} \sin a_{\mathrm{r}})\, \mathrm{e}^{-a_{\mathrm{i}}}, \quad \boldsymbol{f}_s = (\hat{\boldsymbol{f}}_{\mathrm{r}} \sin a_{\mathrm{r}} + \hat{\boldsymbol{f}}_{\mathrm{i}} \cos a_{\mathrm{r}})\, \mathrm{e}^{-a_{\mathrm{i}}} \tag{3.16}$$

and

$$a_{\mathrm{r}} = \int_{x_0}^{x} \alpha_{\mathrm{r}}\, \mathrm{d}x, \quad a_{\mathrm{i}} = \int_{x_0}^{x} \alpha_{\mathrm{i}}\, \mathrm{d}x, \tag{3.17}$$

where the subscripts $_{\mathrm{r}}$ and $_{\mathrm{i}}$ denote real and imaginary part, respectively. The spanwise periodic streaks are taken from optimized solutions of the stability equations (3.2) with $\omega = 0$ and $\alpha = 0$. The forcing vector takes the form

$$\boldsymbol{v}_s = (\hat{u}_{\mathrm{r}} \cos\beta z,\ \hat{v}_{\mathrm{r}} \cos\beta z,\ -\hat{w}_{\mathrm{i}} \sin\beta z). \tag{3.18}$$

The size of the computational box used for the simulations presented in this paper is $(xl \times yl \times zl) = (3.09 \times 206 \times 29.8)$. The width of the box is set to fit one spanwise wavelength of the forced streaks. The Reynolds number at the initial location of the box where $x = 1$ is $Re_\delta = 173$. The resolution is $(nx \times ny \times nz) = (540 \times 541 \times 64)$, which is about 18.7 million points. Dealiasing is activated in the streamwise and spanwise directions. This increases the computational resolution in the simulation with a factor of 2.25 (1.5 in each direction). A shared memory parallelization is implemented in the numerical code. The current study uses 16 nodes, each with two processors. With a wall clock time of 60 h, a typical simulation calculates about one time unit. The parameters for the fringe region are $x_{start} = 3.49$, $x_{end} = 4.09$, $\Delta_{rise} = 0.199$, $\Delta_{fall} = 0.0996$ and $\lambda_{max} = 1.0$.

The waves and streaks are forced in the fringe region in a similar manner to that of Brandt & Henningson (2002), who made use of the same spectral code to study the transition of streamwise streaks in the Blasius boundary layer. The forcing is turned on smoothly in both space and time. The steamwise amplitudes of the waves and streaks are prescribed at the end of the fringe region to 0.001 and 0.03, respectively.

When only two-dimensional waves are forced in the fringe region, random noise is added to the initial field in order to introduce three-dimensionality to the flow. The noise is in the form of Stokes modes, i.e. eigenmodes of the flow operator without the convective term. These modes fulfil the equation of continuity and the boundary condition of vanishing velocity at the wall. While the simulation is running, no more forcing of three-dimensional noise is required since a small level of noise passes through the fringe region. However, the fringe region damps incoming disturbances to an energy level below about $10^{-7}$.

https://doi.org/10.1017/S0022112005005628 Published online by Cambridge University Press

## 4. Results

### 4.1. *Matching the base flow*

Most of the numerical studies of wall jets have concerned the similarity solution of Glauert (1956), which is an asymptotic solution. However, a consideration of the near field of the wall jet in this investigation shows that the flow has not achieved the self-similar Glauert profile. To investigate the flow close to the slot at a rather high Reynolds number, it is necessary to find another base flow more suitable to match with the experiment.

Consider a top-hat profile through a slot with height $b$ located at $x = 0$, see figure 2. Immediately downstream of the slot, a boundary layer develops at the wall and a shear layer develops in the upper part of the top-hat profile, independently of each other. Further downstream, the boundary layer and the shear layer begin interacting and the local maximum velocity slows down. Our solution consists of a coupling of the Blasius boundary layer and the Blasius shear layer as an initial condition to the boundary-layer equations. The two solutions, which are both similarity solutions to the Blasius equation with different boundary conditions, are discussed in Schlichting (1979). In the boundary-layer scalings, the Blasius similarity equation reads

$$2f''' + ff'' = 0, \tag{4.1}$$

where $f(\eta)$ is the non-dimensional streamfunction and the prime denotes derivatives with respect to the similarity variable $\eta$. The base flow can then be written

$$U = f', \quad V = \tfrac{1}{2}(\eta f' - f). \tag{4.2}$$

For the boundary layer, the similarity variable $\eta_b$ relates to the non-dimensional coordinates as $y = \sqrt{x}\eta_b$ and the boundary conditions read

$$\eta_b = 0: \quad f = 0, \quad f' = 0; \qquad \eta_b \to +\infty: \quad f' = 1. \tag{4.3}$$

The shear layer has the displaced similarity variable $\eta_s = \eta_b - b$ and is subject to the boundary conditions

$$\eta_s \to -\infty: \quad f = \eta_s - 2V_b, \quad f' = 1; \qquad \eta_s \to +\infty: \quad f' = 0, \tag{4.4}$$

where $V_b$ denotes the normal component of the free-stream velocity taken from the boundary-layer similarity solution, to fulfil continuity in the normal velocity throughout the wall jet. The two similarity solutions are connected to each other at the location $x = 1$ and form the boundary-layer and shear-layer regions in the Blasius wall jet. The downstream development is computed with the boundary-layer equations. Figure 3 shows the Blasius wall jet and its streamwise development calculated with the boundary-layer equations. The location in figure 3($a$) corresponds to the initial condition at $x = 1$. Figure 3($b$) shows the location $x = 3.14$, where the interaction of the boundary layer and the shear layer has just begun and the maximum velocity is $U_m = 0.99U_0$. Far downstream at the location $x = 20$ (figure 3$c$), the flow approaches the Glauert (1956) solution shown as the dashed line.

In the experiment, thin boundary layers are already formed in the nozzle. Therefore, the virtual slot is placed a distance $l$ upstream of the nozzle outlet with a virtual slot height $b^*$, different from the height of the experimental nozzle opening. In order to match the theoretical base flow to the experiment, $l$, which is taken as the streamwise scale, and $b^*$ have to be chosen. To do so, the boundary-layer and shear-layer regions of the measured wall jet are scaled with local scalings and compared to the Blasius boundary and shear-layer similarity solutions, see figure 4. The experimental data are taken from 1 mm, 6 mm, 11 mm and 16 mm downstream of the nozzle outlet. The

https://doi.org/10.1017/S0022112005005628 Published online by Cambridge University Press

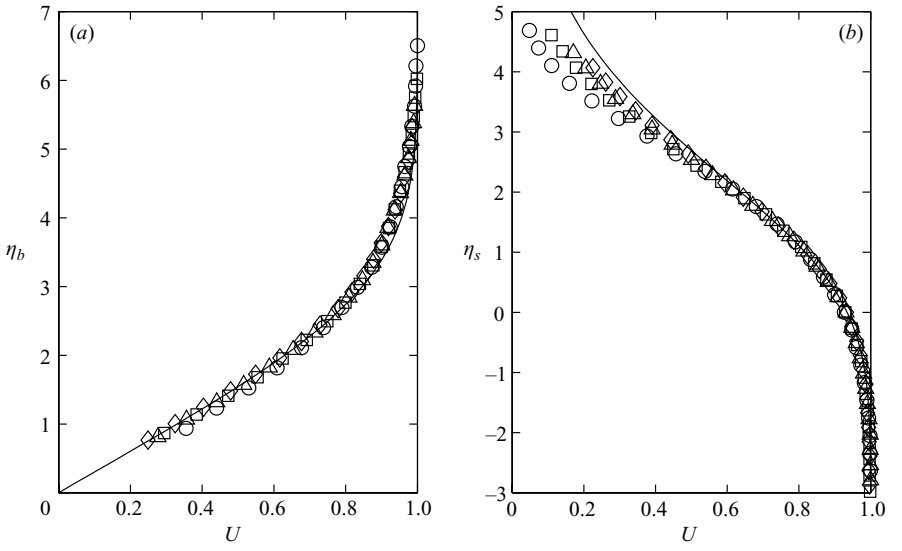



FIGURE 4. Comparison of the computed base flow (—) for $Re_\delta = 173$ with experimental results at 1 mm (○), 6 mm (□), 11 mm (△) and 16 mm (◇) downstream of the nozzle outlet. The experimental data are scaled with the local boundary-layer parameter $\delta$ and local maximum velocity $U_m$ and fitted to the computed similarity solutions with $l = 29$ mm and $b^* = 2.06$ mm. (*a*) Boundary-layer region. (*b*) Shear-layer region.

| | | | | | | | | |
|---|---|---|---|---|---|---|---|---|
| $x$: | 1.0 | 1.03 | 1.21 | 1.38 | 1.55 | 2.0 | 3.14 | 20.0 |
| $x^* - l$ (mm): | 0 | 1 | 6 | 11 | 16 | 29 | 62 | 551 |

TABLE 1. Streamwise locations with the corresponding dimensional distances downstream of the experimental nozzle outlet.

streamwise locations and their corresponding dimensional distances downstream of the experimental nozzle outlet used for the measurements are summarized in table 1. The maximum outlet velocity is $U_0 = 15.4\,\mathrm{m\,s^{-1}}$, corresponding to the Reynolds number $Re_\delta = 173$. The best matching is achieved for $l = 29$ mm and $b^* = 2.06$ mm corresponding to the non-dimensional virtual slot height $b = 12.3$. The normal scale is $\delta = \sqrt{\nu l / U_0} = 0.168$ mm.

The Blasius wall jet can be made independent of the slot height $b$, downstream of the point of interaction of the shear layer and the boundary layer, by introducing the coordinates

$$\zeta = \frac{y}{b}, \quad \xi = \frac{x}{b^2}. \tag{4.5}$$

If we rescale the downstream distance measured from the experimental nozzle opening with the virtual slot height, locations downstream of the point of interaction may be written

$$\frac{x^* - l}{b^*} = Re_\delta \left( b\xi - \frac{1}{b} \right), \tag{4.6}$$

where the star denotes dimensional variables. Inserting the value of the slot height used for our Blasius wall jet, the value of the right-hand side of (4.6) is $1.55 Re_\delta$ at the location shown in figure 3(*c*). Hence, given the top-hat profile blowing out from

https://doi.org/10.1017/S0022112005005628 Published online by Cambridge University Press

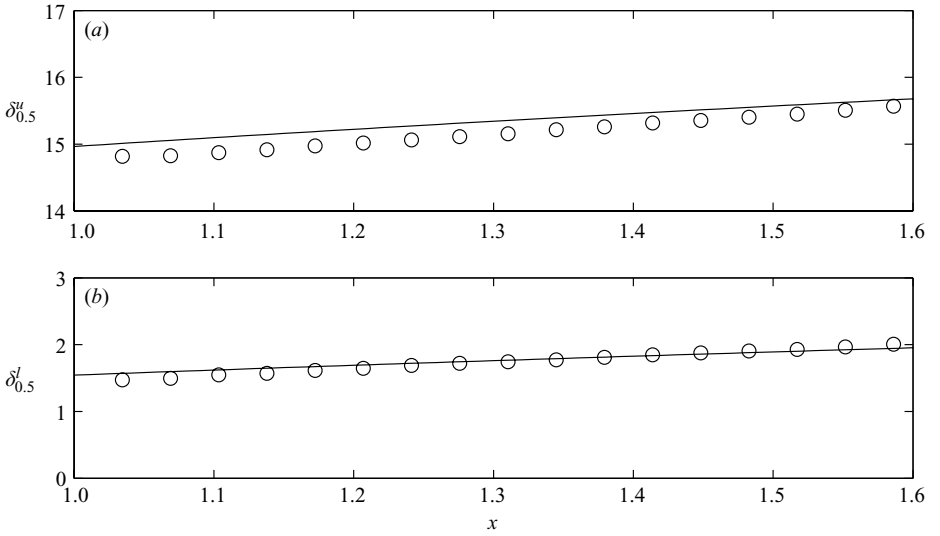



FIGURE 5. Comparison of the computed base flow (—) for $Re_\delta = 173$ with experimental results (○). The graphs show (*a*) the upper and (*b*) lower jet half-widths $\delta^u_{0.5}$ and $\delta^l_{0.5}$, respectively.

a slot, the Glauert wall jet is reachable only many slot height distances downstream of the slot in the case when the flow Reynolds number is high. As the flow Reynolds number decreases, the distance required to approach this solution also decreases. However, given a different initial condition at the slot such as a plane Poiseuille flow, the Glauert wall jet may be reached earlier. Bajura & Szewczyk (1970) experimentally obtain a very good agreement to the Glauert wall jet 18 slot heights downstream of the nozzle outlet for a jet-exit Reynolds number of 377 based on the slot height. Similar results were obtained by Cohen *et al.* (1992) 30 slot heights downstream of the nozzle for a Reynolds number of 725. For comparison, the Reynolds number $Re_\delta = 173$ in this investigation corresponds to 2120 based on the virtual slot height $b^*$, and 3080 based on the height of the experimental nozzle opening.

It can be seen in figure 4 that the agreement between the experiment and the theory in the lower part of the boundary-layer region, shown in figure 4(*a*), and in particular the upper part of the shear-layer region, shown in figure 4(*b*), is not perfect. The experimental data are, however, approaching the theoretical solution further downstream. A slight difference in the upper part of the boundary-layer region remains as the flow evolves downstream. The agreement between the experiment and the theory near the jet core in the shear-layer region is excellent. The main reason for the disagreement in the upper part of the wall jet is the influence of the nozzle. A jump of the boundary condition occurs on the top lip of the nozzle as the flow leaves and a kink in the experimental velocity data can be observed. With increased downstream distance, the influence of the nozzle disappears and the agreement becomes better.

Figures 5(*a*) and 5(*b*) show the streamwise development of the upper and lower jet half-widths $\delta^u_{0.5}$ and $\delta^l_{0.5}$, respectively, which are the distances from the wall where the velocity reaches half the local maximum velocity. The experimental data are measured with 1 mm steps to 17 mm downstream of the nozzle outlet. The whole scaled flow is shown in figure 6 for four downstream locations $x = 1.03, 1.21, 1.38, 1.55$ and the measured upper and lower jet half-widths are indicated with crosses.

https://doi.org/10.1017/S0022112005005628 Published online by Cambridge University Press

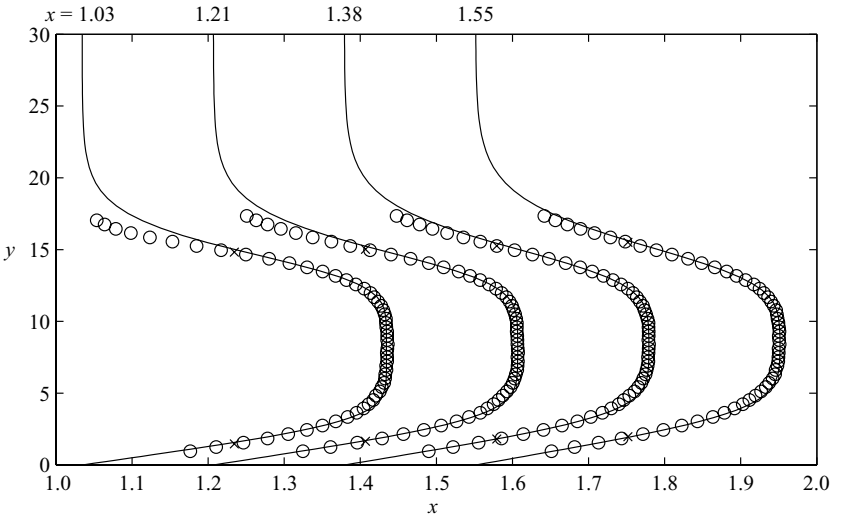



FIGURE 6. Comparison of the computed base flow (—) for $Re_\delta = 173$ with experimental results (○) at 1 mm, 6 mm, 11 mm and 16 mm downstream of the nozzle outlet (the non-dimensional locations are indicated in the figure). ×, upper and lower jet half-widths.

### 4.2. *Linear stability analysis*

In this section, the stability of the computed base flow at $Re_\delta = 173$ is investigated by means of the linear parabolized stability equations and the results are compared with the measurements. The instability with respect to two-dimensional eigenmodes and non-modal streaks is investigated.

#### 4.2.1. *Two-dimensional waves*

The natural spectra of the streamwise velocity component measured in the position of maximum disturbance in the wall-normal direction is shown, at $x = 1.38$ (— — —) and $x = 1.55$ (—), in figure 7(*a*). The reduced frequency is defined as $F = 10^6\omega/Re_l$. It is clear that under natural conditions, the wall jet operates in unforced mode and a broad band of frequencies amplifies. The root mean square of the broadband disturbance amplitude at $x = 1.55$ is approximately 0.5 % of the jet exit velocity. This allows us to consider the flow to be laminar down to this location under natural conditions. Figure 7(*b*) shows the computed physical growth rate, defined as

$$\sigma(x) = \frac{1}{Re_\delta}\frac{1}{\sqrt{\hat{E}}}\frac{\partial\sqrt{\hat{E}}}{\partial x} - \alpha_{\mathrm{i}}, \tag{4.7}$$

versus the reduced frequency. It is clearly visible that in the stability calculations, as well as in the experiment, the most amplified frequency decreases with increased streamwise location. The most amplified frequency of the Blasius shear layer predicted with inviscid stability theory by Monkewitz & Huerre (1982) is about 480, which is very close to the peak observed for the location $x = 1$ in figure 7(*b*). This suggests that the wall jet operates in the shear-layer mode.

Subsequently, the flow is artificially forced in the experiment and characteristics of the instability waves under controlled conditions are studied. The frequency of the artificial disturbances is 1221 Hz corresponding to $\omega = 14.4$, or $F = 482$. This is close to the natural dominating flow frequency, leading to breakdown. In figure 7(*c*), the

https://doi.org/10.1017/S0022112005005628 Published online by Cambridge University Press

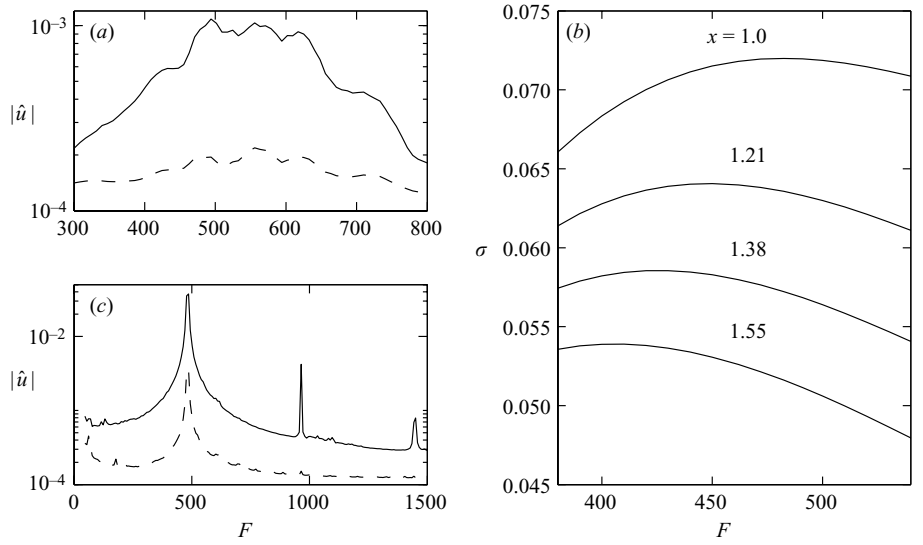



FIGURE 7. Frequency spectra at $x = 1.38$ (— — —) and $x = 1.55$ (—) for natural case ($a$) and forced by a loudspeaker at 1221 Hz ($F = 482$) with amplitude 4 % at $x = 1.55$ ($c$). ($b$) Computed growth rates $\sigma$ for $Re_\delta = 173$ at different streamwise locations corresponding to 0 mm, 6 mm, 11 mm and 16 mm downstream of the nozzle outlet (the non-dimensional locations are indicated in the figure).

forced spectrum, for a relatively large forcing amplitude (4 % at $x = 1.55$) is shown for the same streamwise locations as the natural spectrum. At the location $x = 1.55$, nonlinear effects start to be apparent and peaks of higher harmonics of the main frequency can be seen in the spectra. The first superharmonic has about 10 % of the main harmonic amplitude. The forcing of the flow leads to a strong coherence of the disturbance around the excitation frequency, as can also be seen for free shear layers.

Since the Blasius wall jet is a composition of both a boundary layer and a free shear layer, we should expect the possibility of two co-existing unstable eigenmodes, one associated with the viscous instability of the boundary layer in the inner region and the other with the inviscid instability of the shear layer in the outer region. Mele *et al.* (1986), among others, elaborated the role of these two instability modes of the Glauert wall jet. For the low Reynolds number specified in the current investigation, the PSE-approach does not detect the inner mode, instead it converges to the outer mode. In order to study the inner mode, the Orr–Sommerfeld equation is solved. Thereby, a comparison of the PSE-technique with the parallel theory can also be done. Such comparisons have been made by Bertolotti *et al.* (1992) for the Blasius boundary layer.

Figure 8 shows the streamwise component of Orr–Sommerfeld eigenfunctions at $x = 1$ for $F = 482$ and $Re_\delta = 173$. The inner mode is shown as the solid line in figure 8($a$) while the dashed line shows the corresponding mode of the Blasius boundary layer. As expected, the agreement between the profiles of the two modes is perfect in the inner region close to the wall, whereas two additional small peaks persist in the outer region of the wall-jet mode. In figure 8($b$), the comparison between the outer mode and the corresponding mode of the Blasius shear layer is shown. Here, as expected, the profiles of the modes agree perfectly in the outer region, whereas the wall-jet mode has a small peak in the inner region. However, the agreement between the inner and outer modes of the Blasius wall jet with the corresponding modes of

https://doi.org/10.1017/S0022112005005628 Published online by Cambridge University Press

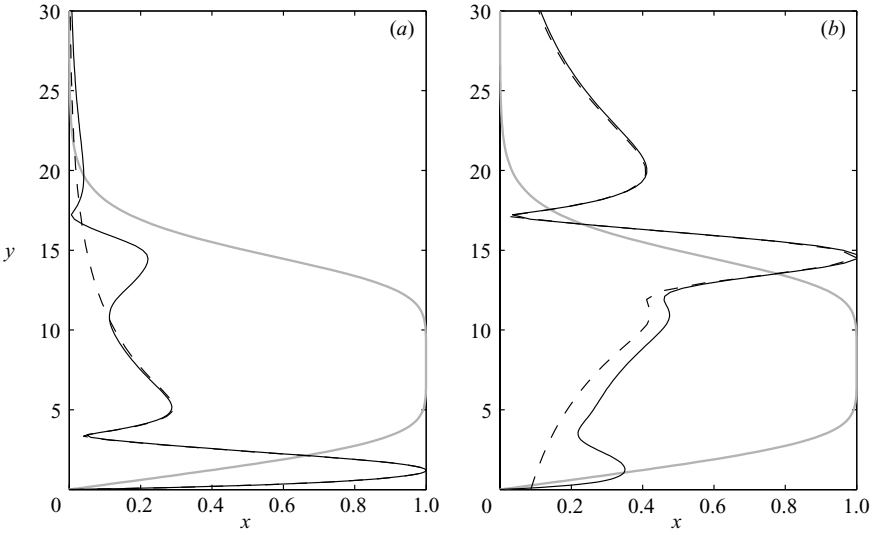



FIGURE 8. Streamwise component of Orr–Sommerfeld eigenfunctions at $x = 1$ for $F = 482$ and $Re_\delta = 173$. The grey line shows the Blasius wall jet. (*a*) Inner mode (—) compared with the corresponding mode of the Blasius boundary layer (– – –). (*b*) Outer mode (—) compared with the corresponding mode of the Blasius shear layer (– – –).

the Blasius boundary layer and Blasius shear layer, respectively, decreases further downstream as the boundary-layer region and the shear-layer region of the Blasius wall jet begin to interact.

At the given Reynolds number and frequency, the outer mode is the only unstable mode of the Blasius wall jet. The critical Reynolds number for the Blasius wall jet is 2.15, this is when the outer mode becomes unstable at $F = 23\,000$. The corresponding critical Reynolds number for the Blasius shear layer is zero. The inner mode becomes unstable at a significantly higher Reynolds number of 272 at $F = 260$. The corresponding critical Reynolds number for the Blasius boundary layer is 302 at $F = 230$. As a comparison, it can be mentioned that the critical Reynolds number for the Glauert wall jet is 13.6 at $F = 9600$.

Figure 9 shows the imaginary part of Orr–Sommerfeld eigenvalues for $Re_\delta = 173$. The inner and outer modes of the Blasius wall jet are shown as solid lines while dashed lines show the corresponding modes of the Blasius boundary layer and the Blasius shear layer, respectively. The streamwise dependency for $F = 482$ is shown in figure 9($a, c$). The inner mode of the Blasius wall jet, shown in figure 9($a$), is stable, but not as stable as the corresponding mode of the Blasius boundary layer. The outer mode, shown in figure 9($c$), is unstable, but the corresponding mode of the Blasius shear layer is slightly more unstable. In both cases, the difference increases downstream. In figure 9($c$), a comparison with the PSE-solution is made. The dots represent each streamwise step of the computation, which is seen to converge at about $x = 0.7$. Downstream of this location the agreement with parallel theory is excellent, indicating that non-parallel effects are small. The local theory seems to slightly underpredict the amplification rate. In order to elaborate the effect of the base-flow disagreement on the stability characteristics, the Orr–Sommerfeld equation is solved for the experimental base flow. First, the experimental base flow is interpolated and extrapolated with continuous first and second derivatives. The imaginary part of the

https://doi.org/10.1017/S0022112005005628 Published online by Cambridge University Press

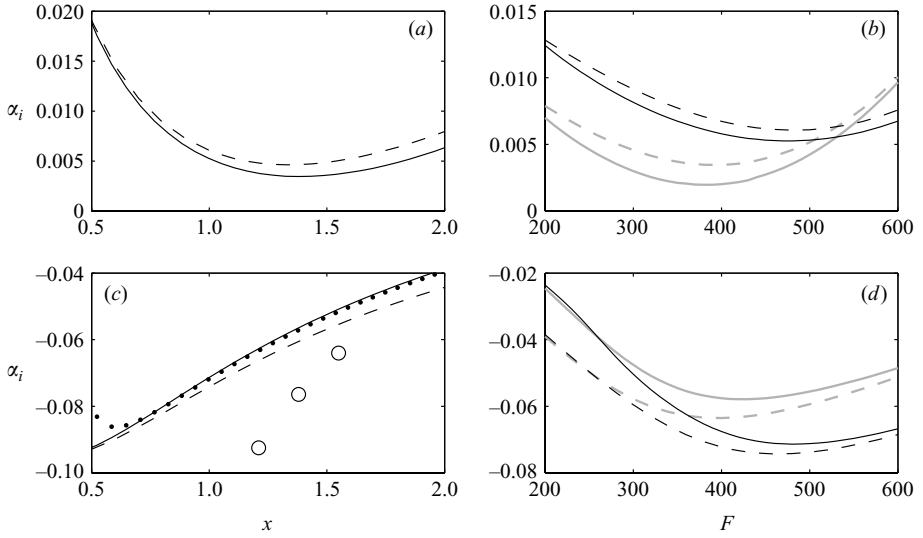



FIGURE 9. Imaginary part of Orr–Sommerfeld eigenvalues for $Re_\delta = 173$. $(a, c)$ Streamwise dependency for $F = 482$. The dotted line in $(c)$ shows a comparison with the PSE-solution. A comparison with the Orr–Sommerfeld solution of the interpolated experimental base flow is also made (○) for $x = 1.21, 1.38, 1.55$. $(b, d)$ Frequency dependency at $x = 1$ (black lines) and $x = 1.38$ (grey lines). $(a, b)$ Inner mode (—) compared with the corresponding mode of the Blasius boundary layer (– – –). $(c, d)$ Outer mode (—) compared with the corresponding mode of the Blasius shear layer (– – –).

streamwise wavenumber at $x = 1.21, 1.38, 1.55$, from these calculations, is shown as the circles in figure 9$(c)$. It reveals a large difference in amplification rate which is due to the disagreement between the shear-layer regions in the measured and the theoretical base flows. The frequency dependency at $x = 1$ (black lines) and $x = 1.38$ (grey lines) of the inner and outer modes is shown in figure 9$(b)$ and 9$(d)$, respectively.

Figure 10 shows the amplitude and phase distribution at three downstream locations $x = 1.21, 1.38, 1.55$ for the three different forcing amplitudes 0.3 % (○), 1.1 % (□) and 1.7 % (△) compared with the computed PSE-results (—). The three experimental amplitude values are measured at the streamwise location $x = 1.55$. It can be noted that the agreement between the experiment and the linear stability computation is acceptable, apart from the upper part of the shear-layer region. The deviation there is most probably because the waves in the experiment are not fully developed eigenmodes this close to the nozzle outlet. Solving the Orr–Sommerfeld equations for the interpolated experimental base flow reveals that the difference in the base flow does not affect the shape of the eigenmodes much. However, the agreement between the outer part of the measured and computed amplitude distributions improves downstream. The disturbance has a typical shape and the peak in the shear-layer region is in antiphase to the peak near the wall in the boundary-layer region.

The downstream development of the disturbances is demonstrated in figure 11$(a)$ and 11$(b)$, where the maximum $u$-velocity amplitude and phase, respectively, are shown versus the streamwise coordinate. The three cases of forcing are compared with the computation and the same symbols are used as in figure 10. The demonstrated amplitude data is normalized with the amplitude at the location $x = 1.21$, and the disturbance phase $\theta_u$ is shown in radians. The agreement in the results between the different forcing amplitudes in figures 10 and 11 indicates the linearity of the

https://doi.org/10.1017/S0022112005005628 Published online by Cambridge University Press

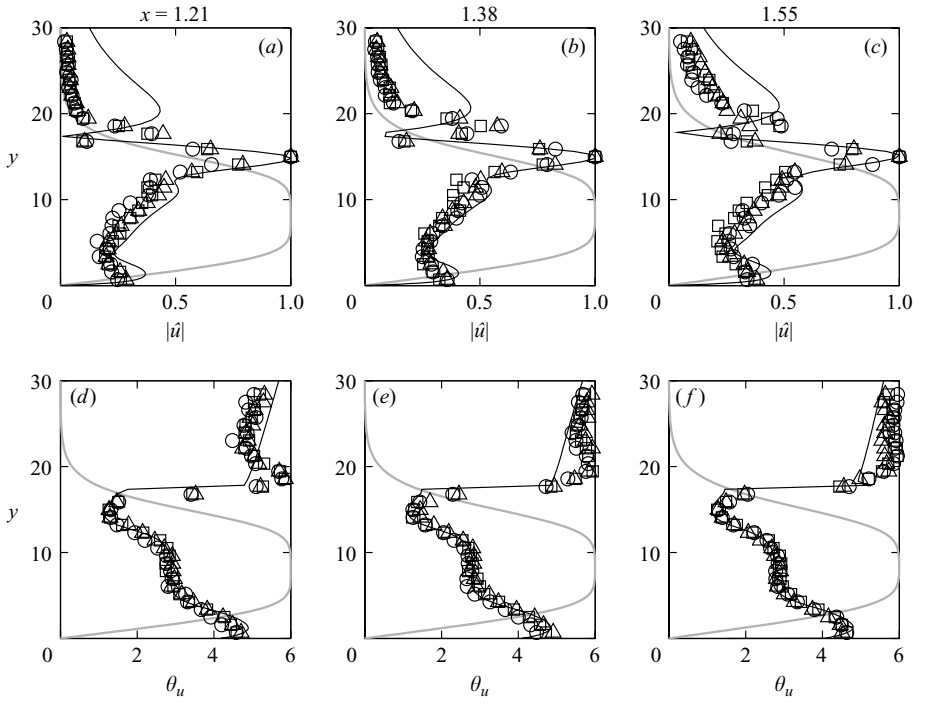



FIGURE 10. Comparison of the computed (—) $u$-velocity amplitude, normalized with its maximum value, and phase distribution $\theta_u$, for $Re_\delta = 173$ and $F = 482$ with experimental results at $x = 1.21, 1.38, 1.55$. The disturbances are triggered by a loudspeaker at 1221 Hz and have the amplitudes 0.3 % (○), 1.1 % (□) and 1.7 % (△) at $x = 1.55$. The grey line shows the computed Blasius wall jet.

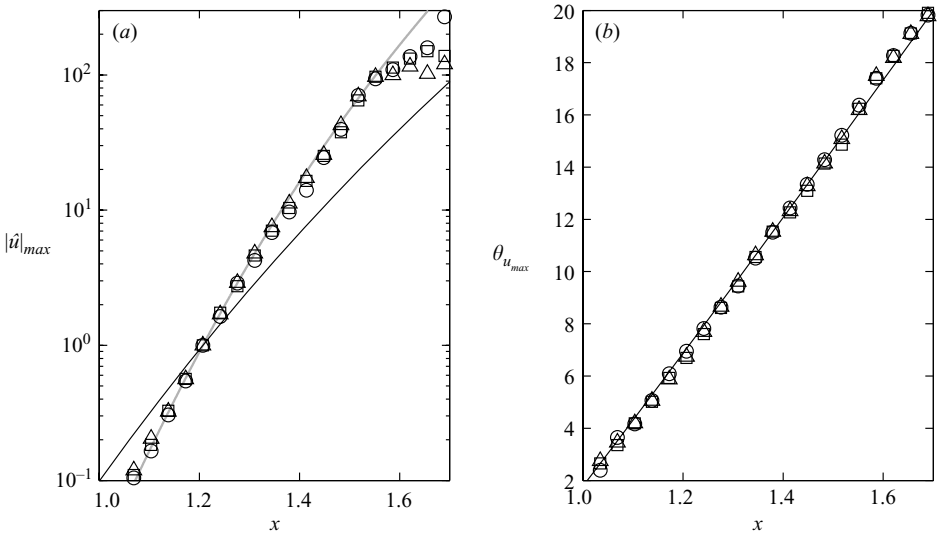



FIGURE 11. Comparison of the computed (—) maximum $u$-velocity amplitude ($a$) and phase ($b$) amplification for $Re_\delta = 173$ and $F = 482$ with experimental results. The disturbances are triggered by a loudspeaker at 1221 Hz and have the amplitudes 0.3 % (○), 1.1 % (□) and 1.7 % (△) at $x = 1.55$. The grey line shows the amplification calculated with the Orr–Sommerfeld equation applied to the interpolated experimental base flow.

https://doi.org/10.1017/S0022112005005628 Published online by Cambridge University Press

disturbance. Both the disturbance distribution and the amplification agree very well for the different forcing amplitudes. An indication of the nonlinear effects appear just after the location $x = 1.55$ where it shows up as lower amplification for the larger forcing amplitudes. The agreement of the amplification between the measured data and the PSE-results showed as the black solid line in figure 11(*a*) is not satisfactory. This difference of the slopes of the amplitude curves implies a 40 % higher growth rate in the experiment, approximately. To investigate how the base flow difference affects the amplification, the Orr–Sommerfeld equation is applied to the interpolated experimental base flow. The amplification, interpolated from the eigenvalues at $x = 1.03, 1.21, 1.38, 1.55$, is shown as the grey line in figure 11(*a*) and the agreement to the measured data is very good. This clearly shows that the difference between the computed and experimental base flow is responsible for the disagreement in amplification between the measured data and the stability calculations.

#### 4.2.2. *Stationary longitudinal streaks*

The exponentially growing disturbances studied in the previous section are the dominating instabilities of flows having a point of inflection. This is true for wall jets as well as for free shear layers operated in a low-disturbance environment. On the other hand, numerous studies of wall-bounded shear flows show that three-dimensional disturbances of a different type may dominate in the breakdown process, especially when the flow is highly disturbed, see e.g. Westin *et al.* (1994). The dominating role of the longitudinal disturbances has been clarified recently by Balaras *et al.* (2001) for highly disturbed free shear layers. As was mentioned in § 1, intermediate states when both two- and three-dimensional disturbances exist are also possible for free shear layers. A similar behaviour is expected for wall jets. In the current experiment, streaks appear naturally from existing irregularities and amplification of vorticity in the contraction. Since such longitudinal structures are also likely to exist in various applications, this is a motivation to study the growth of streamwise streaks.

In the experiment, stationary longitudinal streaks are introduced into the flow by periodically distributed roughness elements that are positioned on the top lip of the orifice. In separate runs, five spanwise scales are generated corresponding to $\beta$ from 0.175 to 0.574 by the roughness elements of corresponding width from 3 to 1 mm. In figure 12(*a*), the spectral decomposition of the maximum streak amplitude for the three largest spanwise scales, $\beta = 0.264$ (○), $\beta = 0.218$ (□) and $\beta = 0.176$ (△), at the streamwise location $x = 1.55$, is shown. The other two smallest scales are decaying in the experiment. One of the introduced scales, $\beta = 0.218$, leads to the disturbance with the largest amplitude and is optimal in this sense. Streaks of approximately this scale are also visible for roughness-unforced flow in the nonlinear stage (see figure 14). These streaks are, however, not stationary, contrary to the forced streaks, they move slowly back and forth.

An idea of how the steady perturbations are selected in the wall-jet flow is directly obtained by considering a plot of the maximized disturbance growth $G_{max}$ versus the streamwise wavenumber. In figure 12(*b*), the computed optimal growth for $\omega = 0$, $x_0 = 0.403$ and $x_1 = 1.55$ is shown as a function of the spanwise wavenumber. The spanwise scale that grows the most is approximately $\beta = 0.29$. In calculations with fixed $x_1$, the optimal spanwise wavenumber decreases with decreased $x_0$. However, for practical reasons, to obtain an initial disturbance in the subsequently described DNS, the initial position is set equal to the starting position of the fringe region. From the comparison of the computed and experimental optimal spanwise scales in figure 12,

https://doi.org/10.1017/S0022112005005628 Published online by Cambridge University Press

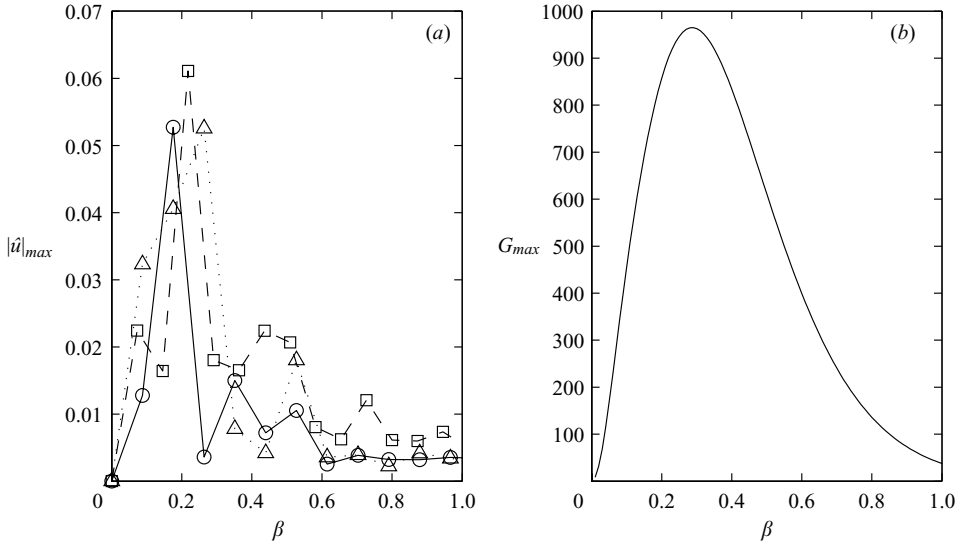



FIGURE 12. (*a*) FFT of three spanwise wavelengths behind arrays of evenly distributed roughness elements with width (half wavelength) 3 mm (○), 2.5 mm (□) and 2 mm (△) from measured streamwise disturbances at $x_1 = 1.55$. (*b*) Computed optimal growth for $\omega = 0$, $x_0 = 0.403$ and $x_1 = 1.55$. $Re_l = 173^2$ is used as the scale factor.

it can be observed that the computed scale is somewhat smaller, however, it is close to that one observed in the experiment.

The optimal disturbance consists of streamwise vortices developing into streamwise streaks. The resulting disturbance from the computation at $x = 1$, for $\beta = 0.211$, $\omega = 0$, $x_0 = 0.403$ and $x_1 = 1.55$, is shown to the left-hand side in figure 13, where one spanwise wavelength of the disturbance is depicted. In figure 13(*a*), the cross-flow velocity components are represented with arrows, and in figure 13(*b*), the streamwise velocity is shown as contours. Positive values of disturbance velocity are shown by solid lines and the dashed lines represent negative values. At the spanwise location $z = 0$, high-momentum fluid is moved up from the jet core, producing a high-velocity streak in the shear-layer region. An opposite motion is observed at the edges of the plot, half a wavelength away, where low-momentum fluid is moved down from the upper velocity field and low-velocity streaks are formed in the shear-layer region. Additionally, in the boundary-layer region, a weak low-velocity streak is formed below the high-velocity streak at $z = 0$, since the upward motion of fluid there carries low-momentum fluid from the wall region. In a similar way, weak high-velocity streaks are formed in the boundary-layer region on the sides. Thus, the more complicated overall character of the disturbance as compared to, for example, the flat-plate boundary layer is explained by rather simple mechanisms, which in general are similar in the single-shear flow of the flat plate and in the wall jet studied here. In figure 13(*c*), the computed (–) normalized streamwise amplitude distribution at $x_1 = 1.55$ is compared with the measured results. The downstream response at the location $x_1$ is insensitive to the choice of spanwise wavenumber and initial position. The similarity between the amplitude functions for the three largest scales in the experiment is also evident in figure 13(*c*). Since the initial condition in the experiment is not the optimal one, we cannot expect to find the calculated disturbance amplitude. However, as long as the initial streamwise vortex in the experiment has a projection on the optimal disturbance, we can expect the final

https://doi.org/10.1017/S0022112005005628 Published online by Cambridge University Press

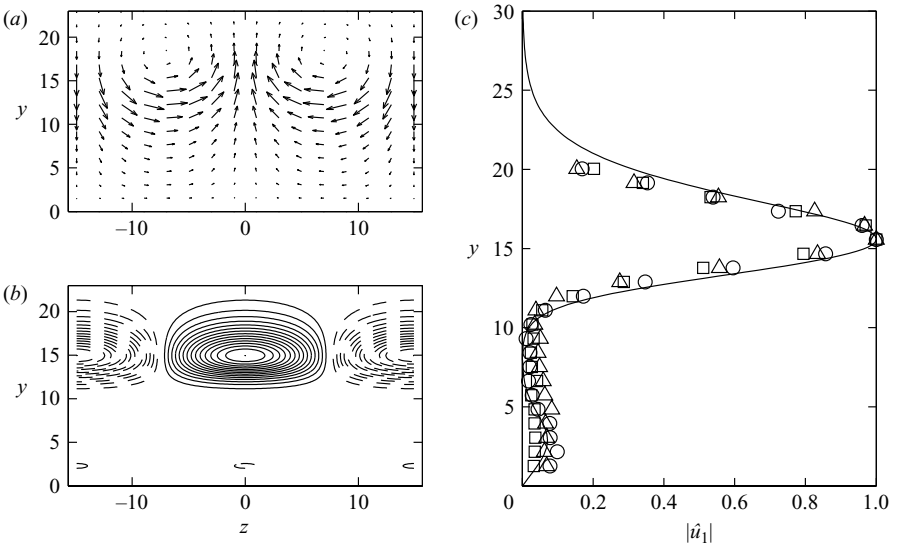



FIGURE 13. Downstream response of the computed optimal disturbance for $\beta = 0.211$, $\omega = 0$, $x_0 = 0.403$ and $x_1 = 1.55$. $(a, b)$ The cross-flow plane at $x = 1$. Arrows represent cross-flow velocity components $(a)$ and contours show constant positive (—) and negative (— — —) streamwise velocity $(b)$. $(c)$ Computed final streamwise amplitude velocity distribution (—), normalized with its maximum value, compared with experimental results for $\beta = 0.176$ (○), $\beta = 0.218$ (□) and $\beta = 0.264$ (△).

computed velocity disturbance to agree with the measured one, as shown in figure 13$(c)$. This agreement and the fact that the computation contains an optimization procedure while the experiment does not, indicate that a fundamental mode is triggered in the flow. This has also been observed by, for example, Andersson *et al.* (1999) and Westin *et al.* (1994) in the flat-plate boundary layer. These non-modal growth mechanisms are referred to as algebraic growth. In the present work, disturbances are triggered by the surface roughness, however, free-stream turbulence is also a possible triggering mechanism, see, for example, Westin *et al.* (1994) for the flat-plate boundary layer results.

### 4.3. *Towards transition to turbulence*

In this section, the transition process of the wall jet is studied. Two-dimensional eigenmodes with the fundamental frequency and non-modal streaks are forced into the flow.

#### 4.3.1. *Overview of the transition process*

The importance of the three-dimensional effects during flow breakdown is clearly demonstrated by the performed flow visualizations, which are shown in figure 14. Two-dimensional waves are excited by the loudspeaker and can be observed to develop parallel to the nozzle edge. A laser sheet is pulsing, synchronized with the wave frequency while smoke is provided into the inlet of the facility driving fan. With this technique, the flow modulation can be visualized only in the top shear layer, where the difference in the smoke concentration is clear. No special forcing is applied to generate three-dimensional disturbances, as they appear naturally from existing irregularities. Nevertheless, well-defined and nearly uniform streamwise vortices and streaks are visibly, forming in the flow. As can be seen in figure 14$(a)$, initially the waves are dominating, while the streaks are rather weak. Further downstream, the streaky structures

https://doi.org/10.1017/S0022112005005628 Published online by Cambridge University Press

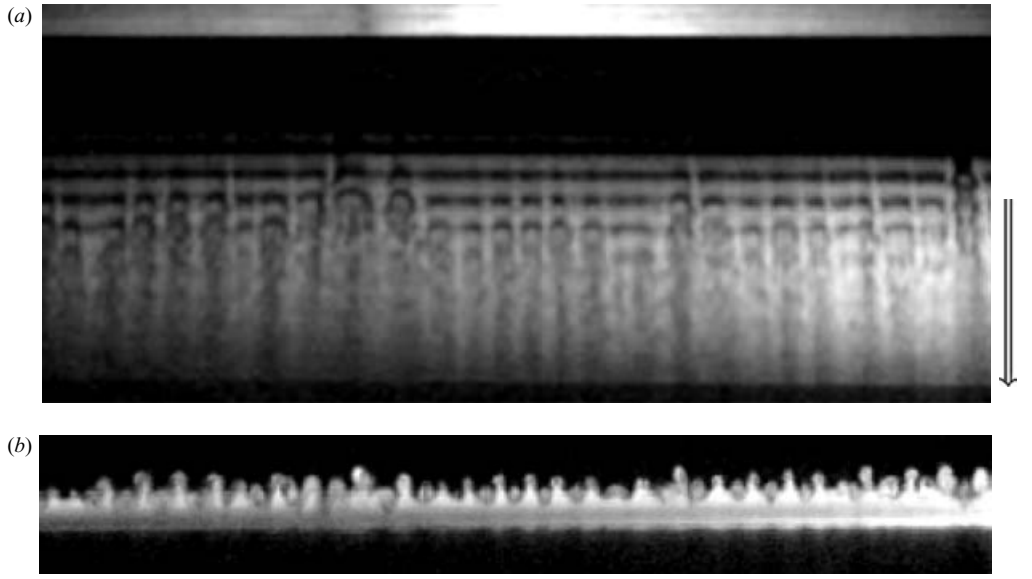



FIGURE 14. Visualization of the nonlinear structures in the wall jet. (*a*) Light sheet is placed parallel to the wall at about 5 mm from it ($y = 30$). The flow direction is down. (*b*) Light sheet is perpendicular to the flow and placed at about 40 mm ($x = 2.3$) downstream of the nozzle outlet.

become dominating. In figure 14(*b*), the braid region of the wave is shown, which corresponds approximately to the mid streamwise location in figure 14(*a*). In the braids, the streaks are well pronounced and they attain a typical mushroom shape. Also, moving the visualization plane further from the wall, regions can be reached where streak tips exist, while waves do not. In fact, the current visualization demonstrates a very similar phenomenon as was observed by Bernal & Roshko (1986) and Lasheras *et al.* (1986) in free shear layers. The streaks in the present case are generated by irregularities in the facility. It is clear that disturbances associated with the streaks are amplified from their upstream origin as the flow develops.

4.3.2. *Spectral analysis*

In the previous section, we saw that the role of the initial conditions for the development of the wall jet is essential. To investigate the process of the breakdown in this flow carefully and understand the nonlinear interactions involved, a direct numerical simulation is necessary. A numerical study conducted in a highly controlled environment is free from various uncontrollable parameters, which make the numerical results more straightforward to interpret than these obtained from the experiment. Two instability modes, the two-dimensional waves and the streamwise streaks are observed to trigger the breakdown of the wall jet to turbulence. These disturbances are excited in the DNS in a controlled manner, as described in § 3.3.2, and the forcing functions are taken from the previously obtained linear stability calculations (see figures 10 and 13). The amplitudes of the waves and streaks are prescribed in the beginning of the computational box to 0.1 % and 3 % of the wall-jet core velocity, respectively. The amplitudes are chosen to obtain a similar transition scenario as in the experimental wall jet seen in figure 14.

The streamwise development of the initially generated modes and the thereafter exited modes of nonlinear interaction can be seen by looking at the development of

https://doi.org/10.1017/S0022112005005628 Published online by Cambridge University Press

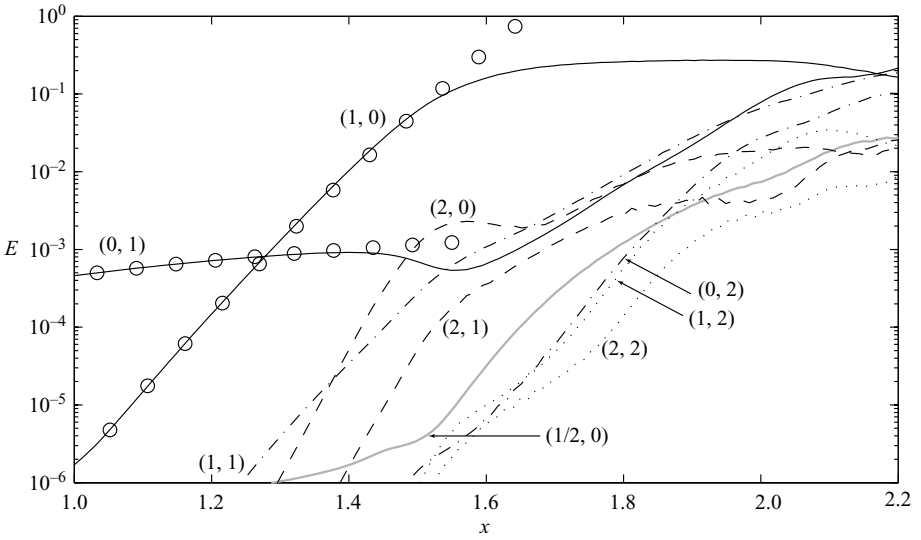



FIGURE 15. Energy in different Fourier modes $(\omega_1, \beta_1)$ from the DNS. The initially excited modes (waves and streaks) are shown by black solid lines, the nonlinearly generated modes are shown by dashed and dotted lines. The modes are indicated in the figure. The pairing mode grows up from numerical noise and is displayed by the thick grey line. Results from the PSE (○) are shown for comparison.

the Fourier components shown in figure 15. For the Fourier transform, 16 evenly distributed velocity fields in time, within two fundamental time periods, starting from $t = 10.95$ are used. Eight modes are used in the spanwise direction. The velocity fields are Fourier transformed in time and in the spanwise direction and the notation $(\omega_1, \beta_1)$, where $\omega_1$ and $\beta_1$ are the frequency and spanwise wavenumber, each normalized with the corresponding fundamental frequency and wavenumber, is used. Thus, the waves and the streaks are represented by (1, 0) and (0, 1), respectively, and are shown as black solid lines in figure 15. Without nonlinear interactions, the instability modes should amplify in agreement with the linear theory and this is observed in the beginning of the computational box, where the waves grow exponentially and the streaks have an algebraic growth. The results from the PSE (○) are shown for comparison and the agreement is excellent. The waves grow according to the linear theory for surprisingly large amplitudes while the nonlinear interactions for the streaks are encountered earlier. It is evident that close to the slot, the two-dimensional effects are dominating over the stronger forced stationary streaks. At about $x = 1.3$ to $x = 1.4$, nonlinear effects start to be apparent when energy is transferred to the modes (1, 1), (2, 0) and (2, 1). Further downstream, the streak mode (0, 1) is decaying and a dip in the energy can be observed at approximately $x = 1.55$. At this location, the time-periodic mode (1, 0) starts to saturate and an abrupt change of the breakdown process happens, namely, an exponential growth of the streak mode.

There are two possible secondary instabilities on two-dimensional vortices generated by inflectional shear-flow instabilities, a subharmonic one leading to vortex pairing, and a three-dimensional one leading to spanwise modulation of the vortices (see e.g. Metcalfe *et al.* 1987). In low-disturbance environments, the predominant secondary instability is associated with vortex pairing. If the initial three-dimensional excitation is large enough, the three-dimensional secondary instability is predominant, resulting

https://doi.org/10.1017/S0022112005005628 Published online by Cambridge University Press

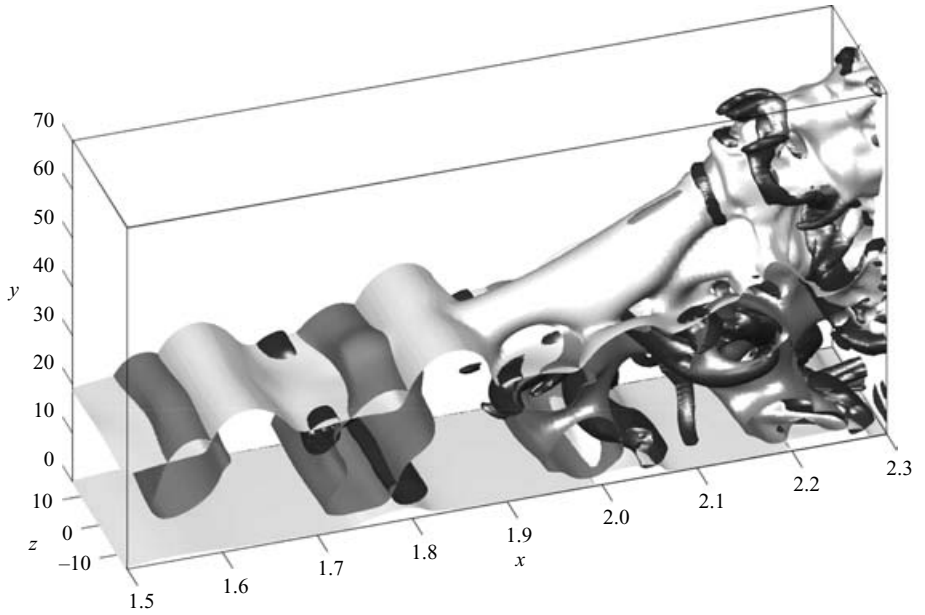



FIGURE 16. Isosurfaces of streamwise velocity (light grey), normal velocity (medium grey) and $\lambda_2$ (dark grey) at an instant of $t = 12.70$. The waves and streaks are forced with initial amplitudes 0.1 % and 3 %, respectively, in the Blasius wall jet for $Re_\delta = 173$. The levels of the isosurfaces are 0.1, 0.1 and −0.015, respectively.

in the growth of a spanwise modulation of the vortices. This results in a suppression of the vortex pairing, and is what can be observed in the current numerical simulation. We have seen that the exponentially growing two-dimensional waves break down owing to what appears to be a three-dimensional secondary instability triggered by the presence of the streaks. In order to asses whether the pairing mode $(1/2, 0)$ is present in the simulation, the energy content in this subharmonic frequency is evaluated and shown as the grey line in figure 15. However, since this mode is not forced (in the fringe region), but only grows out of numerical noise, its amplitude is small. Upstream of the location where nonlinear interactions set in, the amplification rate of the subharmonic mode is about half of the fundamental one. This is consistent with linear theory (see figure 9*d*), indicating that an eigenmode with the subharmonic frequency $F = 241$ is born. At about $x = 1.55$, the amplification rate doubles as a result of nonlinear effects. However, the energy content in this mode stays at least one magnitude below the exponentially growing streak mode.

### 4.3.3. *Flow structures*

From the performed numerical simulation, structures appearing in the flow can be visualized and contribute to an increased understanding of the transition process, complementing the above discussion. In figure 16, positive isosurfaces of the instantaneous streamwise and normal velocity are displayed in light and medium grey, respectively, at $t = 12.70$. Vortical structures can be identified in the flow by plotting regions where the second largest eigenvalue $\lambda_2$ of the Hessian of the pressure assumes negative values (Jeong *et al.* 1997). The vortical structures in figure 16 are represented by dark grey isosurfaces displaying a constant negative value of $\lambda_2$. At the instantaneous moment shown in the figure, the waves are most pronounced in the beginning of the box,

https://doi.org/10.1017/S0022112005005628 Published online by Cambridge University Press

where the waves have already started to saturate. Counterclockwise rotating rollers are moving with the wave troughs in the outer shear layer, of which one is visible at about $x = 1.7$. Slightly downstream of each shear-layer roll-up, clockwise rotating rollers in the boundary layer exist, one of these is visible at about $x = 1.8$. Associated with the boundary-layer rollers are small regions of separated flow. Between the rollers in the outer shear layer and in the boundary layer, inclined regions of upward flow feed the next downstream wave crest. The presence of the streaks deforms the rollers in the spanwise direction. (This is also visualized in figure 20, where only the vortical structures are shown for different instants within one fundamental period.) At about $x = 1.9$, in figure 16, the high-velocity streak becomes dominant and is lifted up from the shear-layer region forming a mushroom-shaped structure. Such structures were also observed by, for example, Wernz & Fasel (1996, 1997) and Gogineni & Shih (1997).

Figure 17 shows six cross-flow slices from the instantaneous flow field presented in figure 16. The arrows represent the cross-flow velocity while the black solid lines show contours of positive streamwise velocity. Contours of negative or zero streamwise velocity are shown by dotted lines. The thick grey lines show the core of vortical structures at the same level of $\lambda_2$ as in figure 16. The first slice, shown in figure 17($a$), is a cut through the boundary-layer roller at $x = 1.8$ and the region of inclined upward flow. A small region of separated flow exists close to the wall. The streak is visible in the outer shear layer where it shows up as a bump in the streamwise velocity contours. This bump is more pronounced in the next slice, depicted in figure 17($b$), which shows a cut through the downward flow at $x = 1.9$. In the slice at $x = 2.0$, shown in figure 17($c$), most of the flow is moving upward and the lift-up of the streak in the ambient flow results in a mushroom-shaped structure. Another small separation bubble can be seen at the wall. The mushroom leg, where the upward motion is strongest, is formed by the combined effect of the upward wave motion and the high-velocity streak. In the top of the upward motion, a vortex pair is forming the mushroom hat. The vortex pair in the mushroom hat separates from its leg and continues upwards through the otherwise mainly downward motion in figure 17($d$), which shows the slice at $x = 2.1$. The breakdown to turbulence is associated with this upper vortex pair. In the slice at $x = 2.2$, shown in figure 17($e$), it can be seen that the outer part of the wall jet is turbulent while the inner part remains organized. However, the turbulence spreads towards the wall further downstream and the flow undergoes transition to a fully turbulent wall jet. Figure 17($f$) shows the slice at $x = 2.3$ where the flow is almost fully turbulent.

Figure 18 allows us to follow the streamwise vorticity in the instantaneous flow field, shown in figure 16, through 12 cross-flow slices. The slices are evenly distributed in space from $x = 1.9$ to $x = 2.35$ and black solid lines show contours of positive streamwise vorticity while contours of negative values are displayed by grey solid lines. The line increment is 0.1, but the zero contour is not shown. In figure 18($c$), the streamwise vorticity associated with the mushroom-shaped structure in figure 17($c$) can be seen. The hat and the leg of the mushroom-shaped structure are indicated in the figure. Further downstream, in figure 18($e$), the hat can be found in the upper part, while the leg splits up and moves with the downward flow towards the edges of the slice. In the slice, shown in figure 18($f$), the first signs of breakdown to turbulence can be seen above the mushroom hat. In the slices, shown in figures 18($g$)–18($j$), the turbulence spreads downward. However, the flow close to the wall is still organized. Through these slides, a $\Lambda$-structure in the boundary layer at the wall can be identified and is indicated with $\Lambda$ in figure 18($i$). Such structures are typical for Klebanoff transition in boundary layers (e.g. Bake, Meyer & Rist 2002). Figure 19 shows the streamwise

https://doi.org/10.1017/S0022112005005628 Published online by Cambridge University Press

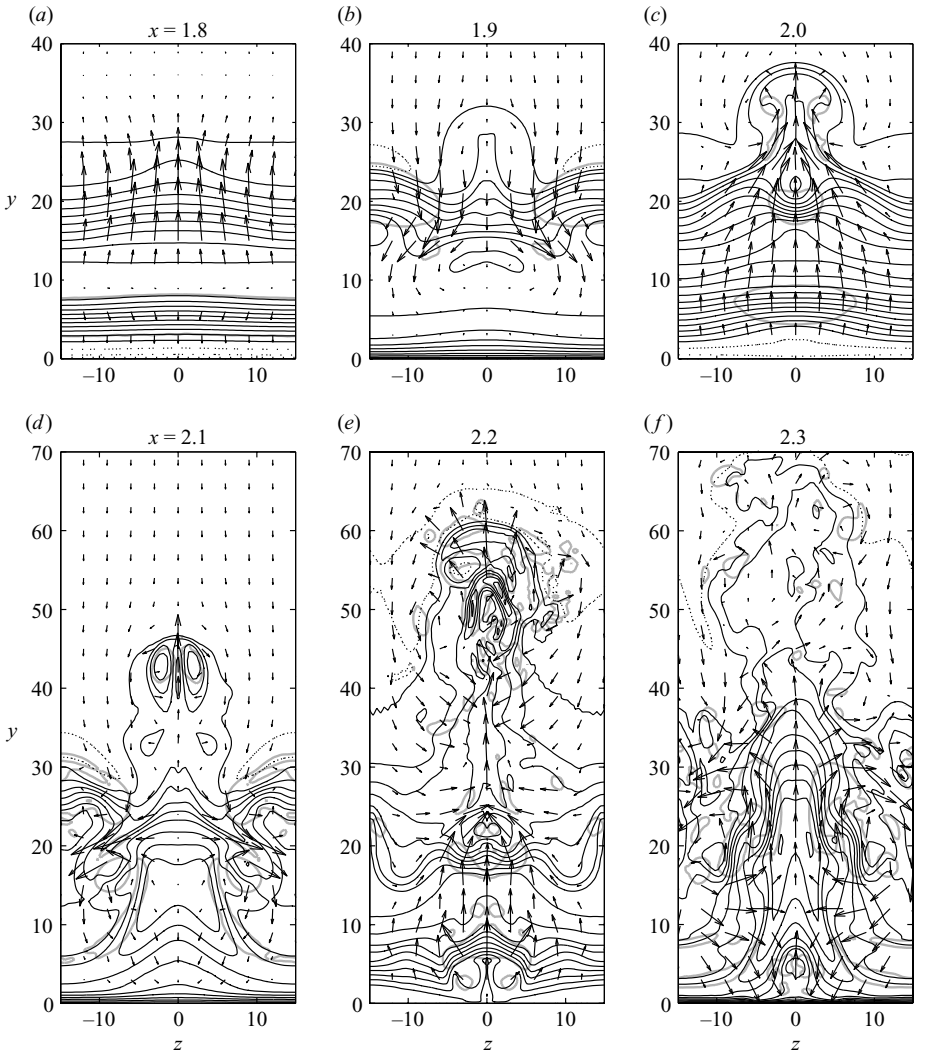



FIGURE 17. Cross-flow planes from the instantaneous data shown in figure 16. Arrows represent the cross-flow velocity while the streamwise velocity is displayed by contours with line increment 0.1. Positive values are displayed by solid lines and negative or zero values by dotted lines. Thick grey lines show the core of vortical structures where $\lambda_2 = -0.015$.

vorticity in a slice parallel to the wall at $y = 20$. It covers a longer region and further demonstrates the three-dimensional flow behaviour and the breakdown to turbulence.

Figure 20 shows the time development of the vortical structures in one fundamental disturbance period starting from $t = 13.31$. The vortex visualization uses instantaneous data from the DNS at six evenly distributed instants. Vortex rollers are moving downstream in the outer shear layer and in the boundary layer. The high-velocity streak in the outer shear layer deforms the roll-up and gives it a bent shape. The corresponding low-velocity streak in the boundary layer induces a bent shape in the opposite direction to the vortex roller in the boundary layer. The interaction between these counter-rotating rollers contributes to the three-dimensional modification of the boundary-layer roller. At the left-hand side of figure 20(*b*), the curved rollers can

https://doi.org/10.1017/S0022112005005628 Published online by Cambridge University Press

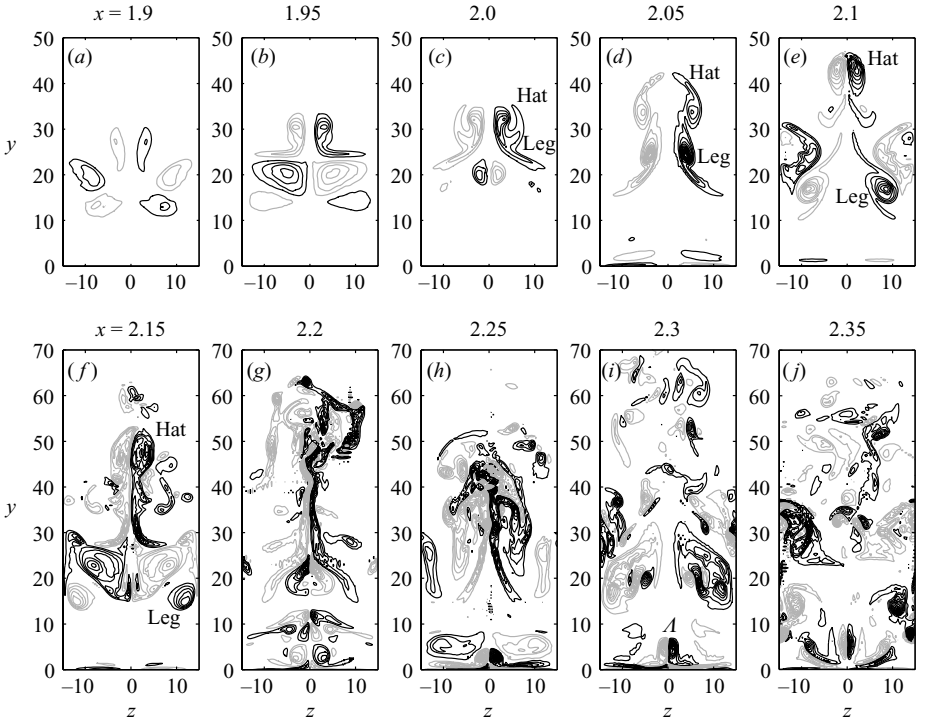



FIGURE 18. Contours of streamwise vorticity in cross-flow planes from the instantaneous data shown in figure 16. The streamwise positions are indicated in the figure. Black lines show positive values and grey lines negative values, the line increment is 0.1, but the zero contour is not displayed.

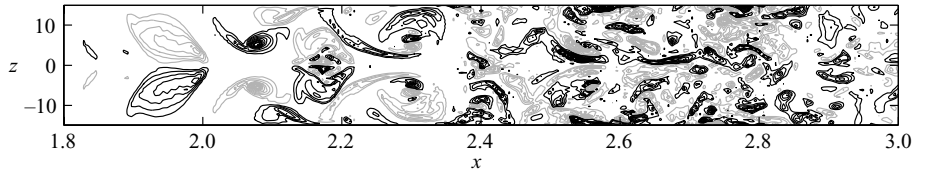



FIGURE 19. Contours of streamwise vorticity in the horizontal plane at $y = 20$ from the instantaneous data shown in figure 16. Black lines show positive values and grey lines negative values, the line increment is 0.1, but the zero contour is not displayed.

be seen. Between the rollers, the flow is pushed upward and forward and inclined rib vortices are created. The rib vortices extend from above the shear-layer roller to beneath the previous one, see figure 20($c$). Such rib vortices have been observed in many experimental and computational studies of mixing layers (e.g. Bernal & Roshko 1986; Lasheras *et al.* 1986; Metcalfe *et al.* 1987; Schoppa, Hussain & Metcalfe 1995). The rib vortices are close together at the tails and wider apart at the tips. At about $x = 2.0$, in figure 20($d$), the upward flow is pushing the rib vortices upward, where they are forming the hat of the mushroom-shaped structure. The tails of the rib vortices, at about $x = 1.9$, keep the normal position. The tails of the previous rib vortices separate around the upcoming rib vortices. Figure 20($d$) shows the instant exactly two fundamental periods after the instantaneous data shown in figures 16–19. The separated legs of the previous rib vortices forms a $\Omega$-shaped vortex ring around

https://doi.org/10.1017/S0022112005005628 Published online by Cambridge University Press

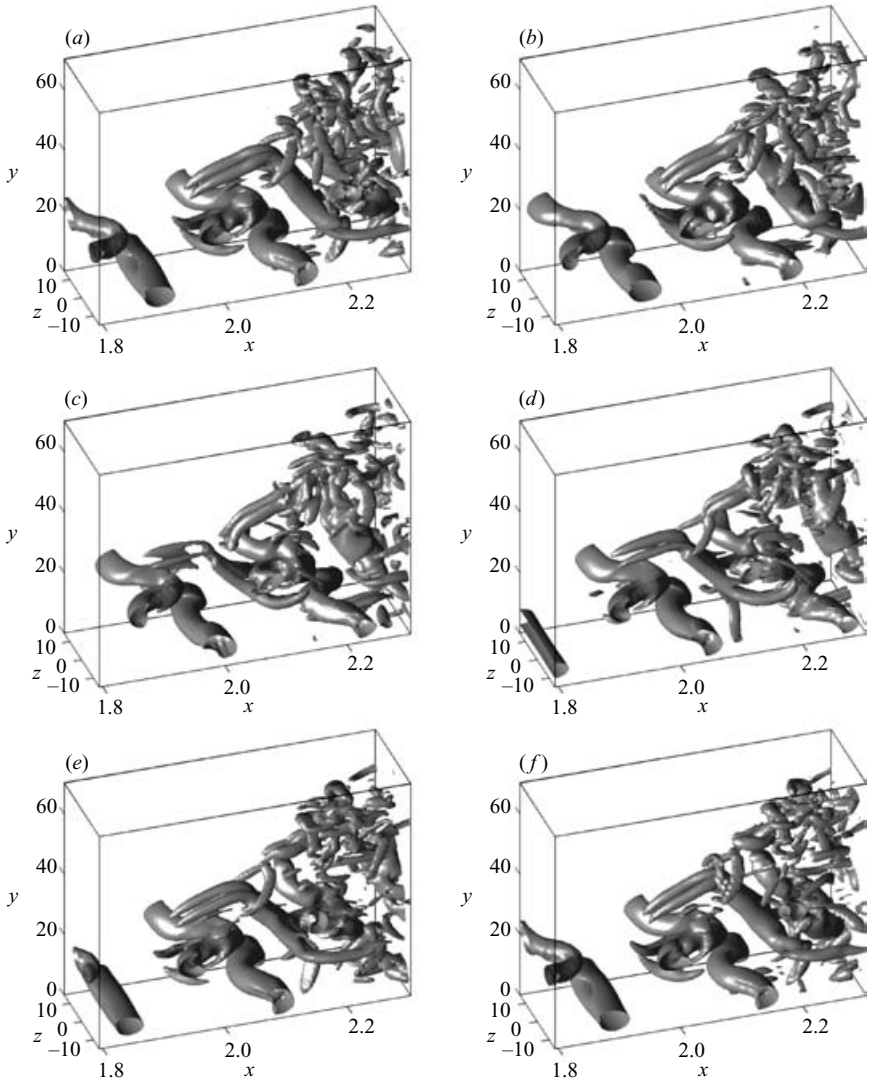



FIGURE 20. Vortex visualization (isosurfaces of $\lambda_2 = -0.015$) using instantaneous data from the DNS at six instants within one fundamental disturbance period $T$: (*a*) $t = 0$, (*b*) $t = 0.2T$, (*c*) $t = 0.4T$, (*d*) $t = 0.6T$, (*e*) $t = 0.8T$, (*f*) $t = T$.

the upcoming rib vortices, see figure 20(*e*). In front of this vortex ring another counter-rotating vortex ring is created (at about $x = 2.1$ in figure 20*f*). The vortex ring formation precedes the breakdown to turbulence. In the end of the lower part of the box, in figure 20(*c*), where the flow is not yet turbulent, the $\Lambda$-structure between the wall and the roller in the boundary layer can be seen.

The coincidence of the numerical visualization with the experimental visualizations of figure 14 is clear; namely, it is seen that in the outer region of the wall jet, the large-amplitude streak structures dominate the late stage of flow breakdown. Both in the computations and in the experiments, a staggered formation of streaks can be observed. The strong three-dimensionality is formed only a certain distance from the nozzle outlet.

https://doi.org/10.1017/S0022112005005628 Published online by Cambridge University Press

### 4.4. *Subharmonic waves and pairing*

In this section, the role of the subharmonic waves is investigated. Two additional simulations are performed, one with the streaks, the fundamental and subharmonic waves forced in the flow and the other with only the fundamental and subharmonic waves and noise in the initial field.

Free mixing layers are known to undergo pairing of the fundamental vortex rollers preceding the breakdown to turbulence (Ho & Huerre 1984; Metcalfe *et al.* 1987; Moser & Rogers 1993; Rogers & Moser 1993; Schoppa *et al.* 1995). Further downstream in the turbulent flow region, spanwise coherent structures may also be observed, where they coexist with fine-scale motion (Konrad 1976). The pairing originates from a subharmonic wave displacing one vortex to the low-velocity region and the next to the high-velocity region. The vortex travelling in the high-velocity region overtakes the slower-moving vortex in the low-velocity region, and pairing appears. The relative phasing of the fundamental and subharmonic disturbances influences the development of the pairing. The three-dimensional modification of the spanwise rollers has been studied numerically by Moser & Rogers (1993), Rogers & Moser (1993) and Schoppa *et al.* (1995) and experimentally by Tung & Kleis (1996). Pairing is found to inhibit the growth of infinitesimal three-dimensional disturbances, and to trigger the transition to turbulence in highly three-dimensional flows. If the amplitude of the initial three-dimensional disturbances is large enough, transition occurs before the pairing takes place. Vortex pairing has also been observed in wall jets (e.g. Bajura & Catalano 1975; Wernz & Fasel 1996).

In order to determine the role of pairing in the Blasius wall jet, the subharmonic disturbance is studied. The Orr–Sommerfeld mode with half the frequency of the fundamental one is forced in the DNS, as described in § 3.3.2. Figure 21 shows the spanwise vorticity in the $(x, y)$-plane at $z = 14.9$ from instantaneous data at $t = 12.70$ for three different forcing cases. Black solid lines show contours of positive spanwise vorticity while contours of negative values are displayed by grey solid lines. The line increment is 0.1, but the zero contour is not shown. In Case 1, shown in figure 21(*a*), streaks and fundamental waves are forced (the simulation described in § 4.3). In Case 2, shown in figure 21(*b*), subharmonic waves are forced in addition to the streaks and the fundamental waves. In Case 3, shown in figure 21(*c*), only fundamental and subharmonic waves are forced. In the absence of the three-dimensional streak, a low level of noise is added to the initial field to introduce three-dimensionality to the flow. The pairing mode is weak in Case 1, as is also seen in the energy content of the corresponding Fourier mode $(1/2, 0)$ in figure 15. In this case pairing does not occur. In Case 2 and 3, the pairing mode is stronger and can be seen as the staggered pattern of the vortex rollers in the outer shear layer. However, in Case 2, pairing does not occur before the breakdown to turbulence. In Case 3, pairing occurs between rollers in the outer shear layer as well as in the boundary layer. Signs of breakdown are first seen in the vortex pair close to the wall in the very end of the box. It can be noted that the vorticity is stronger and breakdown to turbulence is enhanced in the presence of the streak. Figure 22(*a–c*) shows the spanwise vorticity in a cross-flow slice at $x = 2.1$ for the corresponding flow cases. From this figure the difference in the three-dimensional modification becomes clear.

## 5. Summary and conclusion

The dynamics of a plane wall jet is studied using both calculations and experiments. It is found that a laminar wall jet can be successfully described by the solution of

https://doi.org/10.1017/S0022112005005628 Published online by Cambridge University Press

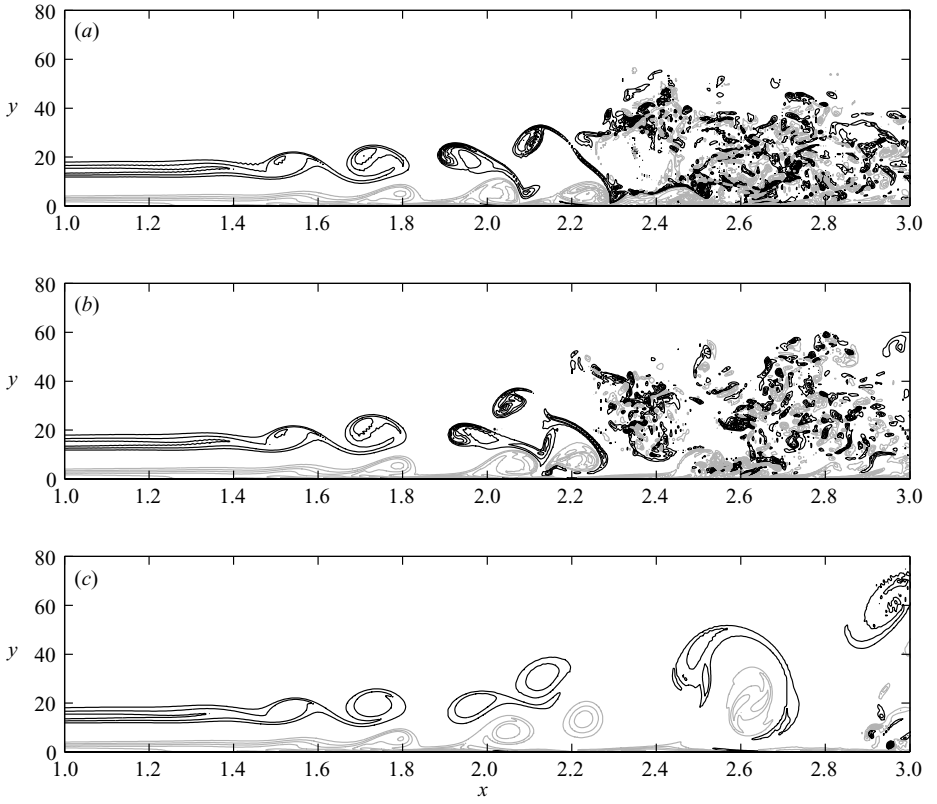



FIGURE 21. Contours of spanwise vorticity in the $(x, y)$-plane at $z = 14.9$. Black lines show positive values and grey lines negative values, the line increment is 0.1, but the zero contour is not displayed. (*a*) Streaks and fundamental waves are forced, same instantaneous data as in figure 16. (*b*) Streaks, fundamental and subharmonic waves are forced. (*c*) Fundamental and subharmonic waves are forced.

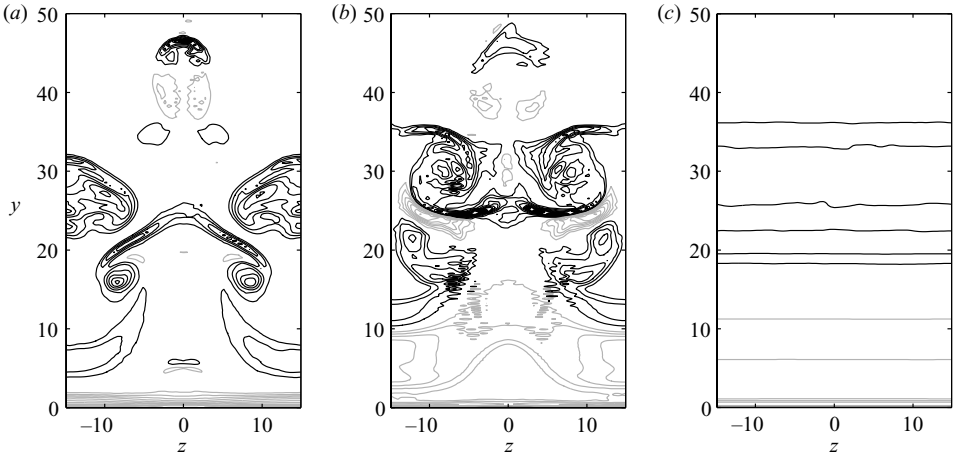



FIGURE 22. Contours of spanwise vorticity in the cross-flow plane at $x = 2.1$ from the instantaneous data shown in figure 21. Black lines show positive values and grey lines negative values, the line increment is 0.1, but the zero contour is not displayed. (*a*) Streaks and fundamental waves are forced. (*b*) Streaks, fundamental and subharmonic waves are forced. (*c*) Fundamental and subharmonic waves are forced.

https://doi.org/10.1017/S0022112005005628 Published online by Cambridge University Press

the boundary-layer equations. The so-called Blasius wall jet, which is matched to the experimental data, is valid in the region just downstream of the nozzle in contrast to the well-known Glauert similarity solution valid further downstream. Comparison of the results of linear stability calculations with experiments shows that the theory is able to predict the most amplified frequency of the periodical waves and the most amplified scale of the streaks. However, the difference in the upper part of the base flow causes an underprediction of the calculated modal amplification. Orr–Sommerfeld calculations demonstrate that the interaction of the two layers of the Blasius wall jet is affecting the stability of both layers. Because of this interaction, the shear-layer part of the jet is stabilized and the boundary-layer part is destabilized. Critical Reynolds numbers are affected in the same manner. The stabilization effect increases with increased interaction between the layers. The local stability approach is shown to work rather well.

In the experiment, streamwise streaks appear naturally in the flow. Linear stability analysis demonstrates a rather large growth of non-modal streaks and this mechanism is responsible for the generation of initial three-dimensionality of the wall jet. Additional support of this conclusion is the excellent agreement between the calculated and measured amplitude functions of the streak. An optimal, most amplified scale exists for the stationary streaks both in the calculations and in the experiment. The calculations indicate that the optimal disturbance represents streamwise vortices, which cause the formation of streaks by the so-called lift-up effect. The mechanism of non-modal growth may affect the selection of scales in the secondary instability of spanwise vortex rollers and thereby the three-dimensional modification preceding flow breakdown.

The nonlinear stage of the laminar flow breakdown is studied with DNS and is experimentally visualized. Three-dimensional simulations with coherent forcing are performed and they clearly demonstrate that growing streaks are important for the breakdown process. It is found that the forcing of streamwise streaks feed into the three-dimensional secondary instability preceding the flow breakdown. As a result, the three-dimensionalities in the flow are enhanced and the other possible secondary instability of the flow, namely the subharmonic pairing of the spanwise vortices, is suppressed. The transition mechanisms can be described by the following stages. (i) Spanwise rollers are formed in the wave troughs in the outer shear layer and move downstream. In the boundary layer close to the wall beneath the wave crests, counter-rotating rollers are formed. (ii) In the presence of streaks, the shear-layer rollers are sinuously modified in the spanwise direction with the boundary-layer rollers deforming in the opposite direction. (iii) Vortex ribs are formed in the braids of the waves, extending from the top of the shear-layer roller to the bottom of the previous one. (iv) The vortex ribs follow the upward flow between two neighbouring shear-layer rollers and are associated with mushroom-shaped structures ejected from the wall jet into the ambient flow. (v) The tail legs of the vortex ribs, generated one fundamental period earlier, separate and form a vortex ring around the upcoming vortex ribs and additional counter-rotating vortex rings are created preceding breakdown to turbulence.

Both the experiment and the DNS reveal that the flow history is extremely important for the transition scenario. In the experiment, the flow is subjected to disturbances already in the apparatus (settling chamber, contraction and nozzle). In the simulations, different forcings of the upstream disturbances lead to different transition scenarios. In order to determine the role of pairing in the Blasius wall jet, the subharmonic disturbance is studied. In total three different forced simulations are performed. (i) Streaks and fundamental waves. (ii) Streaks, fundamental and subharmonic waves. (iii) Fundamental and subharmonic waves and noise. When the subharmonic

https://doi.org/10.1017/S0022112005005628 Published online by Cambridge University Press

disturbance is not forced in the flow, the pairing mode is weak and pairing does not occur. When the subharmonic disturbance is forced, the pairing mode is stronger and can be seen as the staggered pattern of the vortex rollers in the outer shear layer. However, pairing does not occur before the breakdown to turbulence in the presence of streaks. It can also be concluded that vorticity is stronger and breakdown to turbulence is enhanced in the presence of streaks.

This work was funded by the Swedish Energy Agency (Energimyndigheten). The direct numerical simulations was performed at the Center for Parallel Computers at KTH. Many thanks to Mattias Chevalier for the help with various modifications of the spectral code and to Professor Victor Kozlov for the help with the smoke visualizations and for the loan of the laser. Maria Litvinenko has taken part in the experimental measurements which we gratefully acknowledge.

## Appendix. Optimization procedure

In this Appendix, the optimization procedure for the optimal disturbances in the algebraic instability problem is derived. We adopt an input–output formulation of the initial-boundary-value problem (3.2)–(3.4)

$$\hat{u}_1 = \mathscr{A}\boldsymbol{q}, \tag{A 1}$$

where $\mathscr{A}$ is a linear operator. The maximum Reynolds-number-independent growth may then be written

$$\overline{G}_{max} = \max_{\boldsymbol{q}\neq 0} \frac{(\hat{u}_1, \hat{u}_1)_u}{(\boldsymbol{q}, \boldsymbol{q})_q} = \max_{\boldsymbol{q}\neq 0} \frac{(\mathscr{A}^*\mathscr{A}\boldsymbol{q}, \boldsymbol{q})_q}{(\boldsymbol{q}, \boldsymbol{q})_q}. \tag{A 2}$$

Here, $\mathscr{A}^*$ denotes the adjoint operator to $\mathscr{A}$ with respect to the chosen inner product. The maximum of $(\mathscr{A}^*\mathscr{A}\boldsymbol{q}, \boldsymbol{q})/(\boldsymbol{q}, \boldsymbol{q})$ is attained for some vector $\boldsymbol{q}$, which is the eigenvector corresponding to the largest eigenvalue of the eigenvalue problem

$$\mathscr{A}^*\mathscr{A}\boldsymbol{q} = \lambda\boldsymbol{q}, \tag{A 3}$$

where $\overline{G}_{max}$ is the maximum eigenvalue $\lambda_{max}$, necessarily real and non-negative. The most natural attempt to calculate the optimal initial disturbance and its associated maximum Reynolds-number-independent growth is by power iterations

$$\boldsymbol{q}^{n+1} = \mathscr{A}^*\mathscr{A}\boldsymbol{q}^n, \tag{A 4}$$

where the initial disturbance is scaled to the given initial energy in each iteration. To be able to perform the power iterations, we need to know the action of the adjoint operator on $\hat{u}_1$. The following adjoint system can be derived from (3.2)–(3.4) with $\alpha = 0$ and $\hat{p}_x = 0$, by integration by parts

$$-v^*_y + \mathrm{i}\beta w^* = 0, \tag{A 5a}$$

$$-\mathrm{i}\omega u^* - U u^*_x - V_y u^* - V u^*_y + V_x v^* - p^*_x = u^*_{yy} - \beta^2 u^*, \tag{A 5b}$$

$$-\mathrm{i}\omega v^* - U v^*_x - U_x v^* - V v^*_y + U_y u^* - p^*_y = v^*_{yy} - \beta^2 v^*, \tag{A 5c}$$

$$-\mathrm{i}\omega w^* - U w^*_x - V w^*_y + \mathrm{i}\beta p^* = w^*_{yy} - \beta^2 w^*, \tag{A 5d}$$

where $p^*(x, y)$, $u^*(x, y)$, $v^*(x, y)$ and $w^*(x, y)$ are the adjoint variables with boundary conditions

$$\left.\begin{aligned} \overline{u}^* = \overline{v}^* = \overline{w}^* = 0 \quad & \text{at} \quad y = 0, \\ \overline{u}^* = \overline{w}^* = \overline{p}^* + 2V\overline{v}^* = 0 \quad & \text{at} \quad y = y_{max}. \end{aligned}\right\} \tag{A 6}$$

https://doi.org/10.1017/S0022112005005628 Published online by Cambridge University Press

The $x$-derivative in the parabolic set of equations (A 5) has opposite sign compared to (3.2) and the problem has to be solved in the backward direction from the final position $x_1$ to the initial position $x_0$. Therefore, the initial condition is specified at $x_1$

$$\left.\begin{array}{lll} U_1 u_1^* + p_1^* = \hat{u}_1(y) & \text{at} & x = x_1, \\ v_1^* = w_1^* = 0 & \text{at} & x = x_1. \end{array}\right\} \tag{A 7}$$

The action of the adjoint operator is given by

$$\left.\begin{array}{ll} \hat{v}_0 = U_0(y) v_0^*(y) & \text{at} \quad x = x_0, \\ \hat{w}_0 = U_0(y) w_0^*(y) & \text{at} \quad x = x_0. \end{array}\right\} \tag{A 8}$$

The adjoint-based optimization algorithm is very efficient and converges often within three to four iterations, indicating the existence of a well-separated dominating mode.

## REFERENCES


Amitay, M. & Cohen, J. 1993 The mean flow of a laminar wall-jet subjected to blowing or suction. *Phys. Fluids* A **5**, 2053–2057.

Amitay, M. & Cohen, J. 1997 Instability of a two-dimensional plane wall jet subjected to blowing or suction. *J. Fluid Mech.* **344**, 67–94.

Andersson, P., Berggren, M. & Henningson, D. S. 1999 Optimal disturbances and bypass transition in boundary layers. *Phys. Fluids* **11**, 134–150.

Bajura, R. A. & Catalano, M. R. 1975 Transition in a two-dimensional plane wall jet. *J. Fluid Mech.* **70**, 773–799.

Bajura, R. A. & Szewczyk, A. A. 1970 Experimental investigation of a laminar two-dimensional plane wall jet. *Phys. Fluids* **13**, 1653–1664.

Bake, S., Meyer, D. G. W. & Rist, U. 2002 Turbulence mechanism in Klebanoff transition: a quantitative comparison of experiment and direct numerical simulation. *J. Fluid Mech.* **459**, 217–243.

Balaras, E., Piomelli, U. & Wallace J. M. 2001 Self-similar states in turbulent mixing layers. *J. Fluid Mech.* **446**, 1–24.

Bernal, L. P. & Roshko, A. 1986 Streamwise vortex structure in plane mixing layers. *J. Fluid Mech.* **170**, 499–525.

Bertolotti, F. P., Herbert, T. & Spalart, P. R. 1992 Linear and nonlinear stability of the Blasius boundary layer. *J. Fluid Mech.* **242**, 441–474.

Brandt, L. & Henningson, D. S. 2002 Transition of streamwise streaks in zero-pressure-gradient boundary layers. *J. Fluid Mech.* **472**, 229–261.

Chernoray, V. G., Kozlov, V. V., Pratt, P. R. & Löfdahl, L. 2005 Hot wire visualizations of breakdown to turbulence in complex flows. In *Proc. of EUCASS conf.*, pp. 2.11–2.16. Moscow, Russia.

Chun, D. H. & Schwarz, W. H. 1967 Stability of the plane incompressible viscous wall jet subjected to small disturbances. *Phys. Fluids* **10**, 911–915.

Cohen, J., Amitay, M. & Bayly, B. J. 1992 Laminar-turbulent transition of wall-jet flows subjected to blowing and suction. *Phys. Fluids* A **4**, 283–289.

Glauert, M. B. 1956 The wall jet. *J. Fluid Mech.* **1**, 625–643.

Gogineni, S. & Shih, C. 1997 Experimental investigation of the unsteady structure of a transitional plane wall jet. *Exp. Fluids* **23**, 121–129.

Gogineni, S., Shih, C. & Krothapalli, A. 1993 PIV study of a two-dimensional transitional wall jet. *AIAA Paper* 93-2913.

Gogineni, S., Visbal, M. & Shih, C. 1999 Phase-resolved PIV measurements in a transitional plane wall jet: a numerical comparison. *Exp. Fluids* **27**, 126–136.

Hanifi, A., Schmid, P. J. & Henningson, D. S. 1996 Transient growth in compressible boundary layer flow. *Phys. Fluids* **8**, 826–837.

Herbert, T. 1997 Parabolized stability equations. *Annu. Rev. Fluid Mech.* **29**, 245–283.

Ho, C. & Huerre, P. 1984 Perturbed free shear layers. *Annu. Rev. Fluid Mech.* **16**, 365–424.


https://doi.org/10.1017/S0022112005005628 Published online by Cambridge University Press

Jeong, J., Hussain, F., Schoppa, W. & Kim, J. 1997 Coherent structures near the wall in a turbulent channel flow. *J. Fluid Mech.* **332**, 185–214.

Klebanoff, P. S. 1971 Effect of freestream turbulence on the laminar boundary layer. *Bull. Am. Phys. Soc.* **10** (11), 1323.

Konrad, J. H. 1976 An experimental investigation of mixing in two-dimensional turbulent shear flows with applications to diffusion-limited chemical reactions. *Intern. Rep.* CIT-8-PU, California Institute of Technology.

Lasheras, J. C., Cho, J. S. & Maxworthy, T. 1986 On the origin and evolution of streamwise vortical structures in a plane, free shear layer. *J. Fluid Mech.* **172**, 231–258.

Levin, O. & Henningson, D. S. 2003 Exponential vs algebraic growth and transition prediction in boundary layer flow. *Flow, Turb. Combust.* **70**, 183–210.

Li, F. & Malik, M. R. 1994 Mathematical nature of parabolized stability equations. In *4th IUTAM Symp. on Laminar–Turbulent transition, Sendai, Japan* (ed. R. Kobayashi), pp. 205–212. Springer.

Luchini, P. 2000 Reynolds-number-independent instability of the boundary layer over a flat surface: optimal perturbations. *J. Fluid Mech.* **404**, 289–309.

Lundbladh, A., Berlin, S., Skote, M., Hildings, C., Choi, J., Kim, J. & Henningson, D. S. 1999 An efficient spectral method for simulation of incompressible flow over a flat plate. *Tech. Rep.* KTH, Department of Mechanics, Stockholm.

Mele, P., Morganti, M., Scibilia, M. F. & Lasek, A. 1986 Behaviour of wall jet in laminar-to-turbulent transition. *AIAA J.* **24**, 938–939.

Metcalfe, R. W., Orszag, S. A., Brachet, M. E., Menon, S. & Riley, J. J. 1987 Secondary instability of a temporally growing mixing layer. *J. Fluid Mech.* **184**, 207–243.

Monkewitz, P. A. & Huerre, P. 1982 Influence of the velocity ratio on the spatial instability of mixing layers. *Phys. Fluids* **25**, 1137–1143.

Moser, R. D. & Rogers, M. M. 1993 The three-dimensional evolution of a plane mixing layer: pairing and transition to turbulence. *J. Fluid Mech.* **247**, 275–320.

Nordström, J., Nordin, N. & Henningson, D. S. 1999 The fringe region technique and the Fourier method used in the direct numerical simulation of spatially evolving viscous flows. *SIAM J. Sci. Comput.* **20**, 1365–1393.

Rogers, M. M. & Moser, R. D. 1993 Spanwise scale selection in plane mixing layers. *J. Fluid Mech.* **247**, 321–337.

Schlichting, H. 1979 *Boundary-Layer Theory*, 7th edn. Mc-Graw-Hill.

Schoppa, W., Hussain, F. & Metcalfe, R. W. 1995 A new mechanism of small-scale transition in a plane mixing layer: core dynamics of spanwise vortices. *J. Fluid Mech.* **298**, 23–80.

Seidel, J. & Fasel, H. F. 2001 Numerical investigations of heat transfer mechanisms in the forced laminar wall jet. *J. Fluid Mech.* **442**, 191–215.

Tumin, A. & Aizatulin, L. 1997 Instability and receptivity of laminar wall jets. *Theoret. Comput. Fluid Dyn.* **9**, 33–45.

Tung, S. & Kleis, S. J. 1996 Initial streamwise vorticity formation in a two-stream mixing layer. *J. Fluid Mech.* **319**, 251–279.

Visbal, M. R., Gaitonde, D. V. & Gogineni, S. P. 1998 Direct numerical simulation of a forced transitional plane wall jet. *AIAA Paper* 98-2643.

Wernz, S. & Fasel, H. F. 1996 Numerical investigation of unsteady phenomena in wall jets. *AIAA Paper* 96-0079.

Wernz, S. & Fasel, H. F. 1997 Numerical investigation of forced transitional wall jets. *AIAA Paper* 97-2022.

Westin, K. J. A., Boiko, A. V., Klingmann, B. G. B., Kozlov, V. V. & Alfredsson, P. H. 1994 Experiments in a boundary layer subjected to free stream turbulence. Part 1. Boundary layer structure and receptivity. *J. Fluid Mech.* **281**, 193–218.

https://doi.org/10.1017/S0022112005005628 Published online by Cambridge University Press